Materials Today Chemistry 47 (2025) 102776

Contents lists available at ScienceDirect

Materials Today Chemistry

journal homepage: www.journals.elsevier.com/materials-today-chemistry/

Exploring X-ray total scattering and pair distribution functions for local structure analysis of single-atom catalysts on polymeric supports

Isabella Kappel [a,b,c], Maxwell W. Terban [d], Maurice Vennewald [b], Nina M. Sackers [b], Andree Iemhoff [b], Janine C. Baums [b], Sebastian Leiting [a], Martin Etter [e], Peter J.C. Hausoul [b], Regina Palkovits [b,c,f,*], Claudia Weidenthaler [a,**]

[a] Department of Heterogeneous Catalysis, Max-Planck-Institut für Kohlenforschung, Kaiser-Wilhelm-Platz 1, 45470, Mülheim a.d. Ruhr, Germany
[b] Institut für Technische und Makromolekulare Chemie, RWTH Aachen University, Worringerweg 2, 52074, Aachen, Germany
[c] Institute for a Sustainable Hydrogen Economy, Forschungszentrum Jülich, Marie-Curie-Str. 5, 52428, Jülich, Germany
[d] Max-Planck-Institut für Festkörperforschung, Heisenbergstraße 1, 70569, Stuttgart, Germany
[e] DESY, FS-PETRA-D, P02.1, Notkestraße 85, 22607, Hamburg, Germany
[f] Max-Planck-Institute for Chemical Energy Conversion, Stiftstr. 34-36, 45470, Mülheim a.d. Ruhr, Germany

ARTICLE INFO

Keywords:
Single-atom catalysis
Polymers
In situ characterization
Difference pair distribution function analysis
X-ray photoelectron spectroscopy

ABSTRACT

The local structure analysis of low-loaded single-atom catalysts on polymeric supports conflicts with the detection limit of analytical methods due to the low metal contents (≤0.5 wt%) and the disordered character of the supports. However, understanding the structure on an atomic level is the precondition to draw structure-property-relationships. In this study, we demonstrate that X-ray total scattering and subsequent atomic (difference) pair distribution function analysis (dPDF) have the potential to contribute in that regard. Atomic pair correlations related to the coordination environment of highly dispersed metal centers as well as structural information of the polymeric support materials could be extracted. Different coordination environments of the isolated species depending on the metal precursor could be observed. *In situ* dPDF analysis allowed to track the dynamic behavior of initially site-isolated Pd species on exfoliated graphitic carbon nitride under reaction conditions making it a suitable method to study their stability. Complementary quasi *in situ* XPS analysis confirmed the observation of increasing Pd–Pd pair correlations by indicating the formation and growth of Pd clusters/nanoparticles during the course of reaction. We discuss the system feasibility, limitations of the method and benchmarking of measurement protocols providing practical guidance for sample preparation, measurement conditions and their impact on the data quality during the analysis of low-loaded single-atom catalysts.

1. Introduction

A transformation of the chemical industry is required to reach the desired climate goals. Heterogeneous catalysis presents one of the key technologies to enable the indispensable shift to a circular economy as a prerequisite of a sustainable society. Consequently, research on the development of efficient catalytic processes is of major importance. Single-atom catalysis offers the possibility to contribute in that regard, as it combines advantages of both heterogeneous and homogeneous catalysis such as unique reactivity and good separation and handling properties that are important for recycling [1]. Furthermore, they also enable maximum utilization of rare and expensive metals [2]. In order to design more efficient catalytic systems, detailed material characterization is of utmost importance to understand structure-property relationships on an atomic level.

From a characterization point of view, some fundamental questions arise when discussing single-atom catalysis. In the first place, this includes being able to prove the presence of site-isolated atomic species and further determining how the coordination environment influences the catalytic reactivity [3–5]. It is also helpful to better understand how the chosen support material immobilizes the metal complexes to stabilize the single metal species and prevent agglomeration, especially

* Corresponding author. Institut für Technische und Makromolekulare Chemie, RWTH Aachen University, Worringerweg 2, 52074, Aachen, Germany.
** Corresponding author. Department of Heterogeneous Catalysis, Max-Planck-Institut für Kohlenforschung, Kaiser-Wilhelm-Platz 1, 45470, Mülheim a.d. Ruhr, Germany.
E-mail addresses: palkovits@itmc.rwth-aachen.de, r.palkovits@fz-juelich.de (R. Palkovits), weidenthaler@mpi-muelheim.mpg.de (C. Weidenthaler).

https://doi.org/10.1016/j.mtchem.2025.102776
Received 9 December 2024; Received in revised form 15 May 2025; Accepted 23 May 2025
Available online 5 June 2025

under reaction conditions. Furthermore, it is known that the support material can act as a macro ligand influencing charge transfer and density with respect to the active metal and consequently tune the catalytic reactivity [6–8].

Various techniques are traditionally used to assess these properties. The development of aberration-corrected scanning transmission electron microscopy has enabled the depiction of single metal atoms and site-isolated supported metal complexes [9–13]. The method probes the sample very locally, and a clear distinction between single atoms, clusters and particles is facilitated by good contrast between support and metal species. However, the high-energy electron beam causes movement and alteration of the sample under investigation, complicating data acquisition [14] and it is difficult to develop quantitative models based solely on this method. Furthermore, X-ray absorption spectroscopy including extended X-ray absorption fine structure spectroscopy (EXAFS) and X-ray absorption near edge spectroscopy (XANES) have proven to be of great value [3,15–19]. While XANES allows determining the oxidation state, EXAFS data provide the basis for the modelling of the direct coordination environment of atoms [17] even for dilute samples [20]. Both methods are bulk average techniques and are element specific, as the measurements are conducted at the absorption edge of the respective metal atom of interest. However, XAS beamlines are typically not set up to cover the energy ranges relevant to the edges of the atoms in the support materials. Thus, multiple measurements are needed to access the coordination environment of different elements in the system. The information obtained is limited to only the first few coordination shells around the investigated atom.

In catalytic materials, the surface is of especially high interest. X-ray photoelectron spectroscopy (XPS) probes the support material's surface structure, potential coordination sites, and electronic structure of immobilized metal species. Therefore, it can contribute to determining metal nuclearity. However, a lack of suitable references makes detailed XPS fitting challenging as the binding energy is highly influenced by the local coordination environment [21]. Mostly it is used to exclude the presence of metallic species and confirm the presence of metal ions. XPS is reported to be sensitive to the electronic structure but less sensitive to the environment, while XAS offers better possibilities to determine the coordination sphere but is limited to the electronic structure in single-atom catalysts [16].

Other methods such as nuclear magnetic resonance (NMR) or Raman spectroscopy can give insights on chemical environment and metal-carrier interactions but require high metal loadings [7]. Infrared spectroscopy has the potential to study the adsorption of probe molecules on single atoms or nanoparticles by characteristic vibration modes but is not suitable for carbon-based systems [7,22]. Analysis of single-atom catalysts is further complicated if the support structure is disordered or amorphous. Inhomogeneity offers various coordination possibilities for the immobilization of metal species and accordingly, results in a variety of slightly differing metal coordination environments. Therefore, comparing experimental data with reference materials with defined and known coordination environments is of high importance, irrespective of the applied method. Additionally, single-atom catalysts typically possess very low metal contents in order to prevent metal agglomeration and maintain isolated sites, which again adds difficulties during analysis as the metal content approaches the detection limit of many characterization techniques. Consequently, oftentimes only assumptions about the predominant species are made. However, it should be mentioned that Hai et al. have successfully demonstrated the synthesis of ultra-high-density single-atom catalysts with metal loadings up to 23 wt % [23]. Experimental data can be further supported by computational simulations such as density functional theory (DFT) or Monte Carlo calculations. Such studies can be used to predict the most likely coordination environment by calculating metal core level binding and formation Gibbs energies [2,24].

The aforementioned techniques still leave open questions and space for additional complementary methods to gain insights on the local atomic environment. For that reason, the applicability of X-ray total scattering and subsequent (difference) pair distribution function (PDF) analysis to give complementary structural details on single-atom catalysts shall be investigated in this study. PDF analysis can provide local structural information for amorphous, nanostructures and dilute systems as it does not require lattice periodicity [25,26]. In particular, the difference PDF (dPDF) method has proven to be a suitable characterization technique as the scattering contribution of the component of interest can be isolated even for very low concentrations [27–29] and therefore offers opportunities for the characterization of single-atom catalysts. This method has been successfully applied to the characterization of several classes of materials. Chapman et al. have demonstrated the use of differential PDF analysis to study the dynamic host-guest interactions in a nanoporous Prussian Blue [30] and H_2-framework interactions in a Prussian Blue analogue [31]. Another example is the extraction of host-guest interactions in MOFs [32–34]. Also in heterogeneous catalysis scientists have demonstrated the usefulness of PDF and dPDF analysis to obtain local and long-range structural information especially with respect to the formation and growth of supported nanoparticles [35,36]. It has been shown that it is possible to study the behavior of small Au and Ag clusters during thermal activation via dPDF analysis [37]. The changes in the interatomic distances at different temperatures allowed to draw conclusion about particle migration, coalescence and reconstruction. Chupas et al. have applied the dPDF analysis to monitor the formation and growth of Pt nanoparticles starting from $PtCl_6^{2+}$ ions in an reducing atmosphere on a TiO_2 support [38]. The Pt loading in these experiments was varied from 2.5 to 7.5 wt % [38,39]. Newton et al. tracked the catalytic activity and related local structure changes of small Pt nanoparticles (1 wt%) on Al_2O_3 via dPDF analysis during CO oxidation [40]. Furthermore, this characterization method has been used for the analysis of the local structure of isolated palladium sites on layered covalent organic frameworks (COF) [41]. Apart from Pd nanocrystals, the group was able to detect the presence of $Pd^{II}Br_2$-moieties in the catalysts. The amount of Pd loaded onto the COF was reported to be $>$ 10 wt% and the COFs themselves retained crystallinity after metalation. Very recently *in situ* dPDF analysis was used to study sintering resistant single-site catalysts in a polyoxometalate (POM) -metal-organic-framework architecture [42]. Local structure transformations of POMs during annealing to the active clusters could be tracked. In an alternative to X-ray-based PDF analysis, electron PDF (ePDF) has been successfully employed to investigate the local structure of nanocarbon-supported Pt under reaction conditions [43]. Clear electron difference PDFs could be obtained for a metal loading down to 3 wt% Pt, which allowed to follow the detachment of Cl^- and the aggregation to clusters at different temperatures.

Compared with other methods PDF (and dPDF) analysis enables access to structural information on different length scales based on one measurement, covering the possibility to analyze the polymeric support materials, immobilized nanoparticles and simultaneously the coordination environment of single-atoms. Furthermore, PDF analysis is not limited to analyzing one element at a time and the obtained bond distances are absolute [38]. Obtaining absolute bond distances is also a viable proposition based on EXAFS data. However, via PDF analysis they are accessible more intuitively and without the need for model structures and performing subsequent intensive fitting procedures. This approach is of particular benefit in the context of small targets in complex chemical environments. In single-atom catalysis carbon-based polymeric materials containing nitrogen and phosphorous heteroatoms, have proven to be good support structures for the immobilization of isolated metal complexes as well as suitable macroligands influencing catalytic properties [7,16]. The characterization of these systems is however challenging due to the above-mentioned circumstances such as low metal loadings and disordered/amorphous support structures composed of weakly scattering elements. For this work we have focused on the analysis of single-atom catalysts based on three structurally different polymeric support materials namely, covalent triazine

frameworks (CTF) [22,44], exfoliated graphitic carbon nitrides (ECN) [14] and polyphosphines [45–48]. The schematic structure units and building blocks of the polymeric support materials are shown in Fig. 1. Furthermore, the figure depicts potential coordination scenarios [14,49] for the immobilized metal atoms. An overview on the characterized material systems containing further structural information and the respective sample name abbreviation are given in Tables 1 and 2.

Throughout this study, we will describe how local structure information of the different polymeric supports and especially of site-isolated metal species in single-atom catalysts can be accessed on the basis of X-ray total scattering data. In addition, we would like to provide relevant practical guidance for the data collection and processing that is suitable for practitioners without extensive experience of X-ray total scattering experiments and dPDF analysis.

2. Materials

The polymeric support materials studied in the framework of this project include layered materials such as exfoliated graphitic carbon nitride (ECN) and covalent triazine frameworks (CTFs). The CTFs discussed here can be subdivided into A-CTFs and Z-CTFs dependending on their synthesis route and corresponding structural characteristics. While the A-CTFs were synthesized via a low-temperature polycondensation (amidine-route) method, the Z-CTFs were synthesized via a high-temperature ionothermal ($ZnCl_2$-route) method. Consequently, A-CTFs represent non-carbonized CTFs while Z-CTFs represent carbonized CTFs. Based on earlier studies it is known that A-CTFs are characterized by a higher nitrogen content indicating the less pronounced degree of carbonization compared with Z-CTFs. Furthermore, the lower degree of carbonization due to the avoidance of high temperatures and the avoidance of $ZnCl_2$ during the synthesis process results in CTFs with a more ordered framework but an ill-defined pore network [44]. The XRD data of the A-CTF resembles the data published on the CTF synthesized by Kuhn et al. (Fig. S4) [50]. The CTF described in their work is distinguished by its markedly low surface area and reflections that closely resemble those of the idealized structure, which exhibits hexagonal AAA packing and layered aromatic sheets. Due to the increased degree of carbonization in the Z-CTFs it is known that these materials deviate from an idealized structure (Fig. 1b) and contain lower amounts of nitrogen [22,49,50]. Furthermore, it was reported that CTF synthesized via the $ZnCl_2$-route show a well-defined mesoporosity and a very high surface area [51]. Another class of support materials for single-atom catalysts are phosphorous containing polymeric supports [45–48]. The polyphosphines were prepared using different linkers and different bridges connecting the phosphorous anchoring sites (Fig. 1). They can also be subdivided depending on the type of linker (L) and polyphosphine bridge (B) that was used during their synthesis and resulted in the polyphosphines P1, P3 and P4. Table 1 summarizes the

Table 1
Support materials abbreviations and material information.

Abbreviation	Support material information
ECN	Exfoliated graphitic carbon nitride
Z-CTF	High-T, ionothermal $ZnCl_2$-route based, carbonized covalent triazine framework
A-CTF	Low-T, polycondensation amidine-route based, non-carbonized covalent triazine framework
P1	Polyphosphine L1+B1
P3	Polyphosphine L1+B2
P4	Polyphosphine L2+B2

Table 2
Catalyst sample abbreviations and material information.

Abbreviation	Catalyst information
ECN-Pd-0.5-SA-NO_3	0.5 wt% Pd single-atoms @ ECN, Pd-Precursor: $Pd(NH_3)_4(NO_3)_2$
ECN-Pd-0.5-SA-Cl	0.5 wt% Pd single-atoms @ ECN, Pd-Precursor: K_2PdCl_4
ECN-Pd-0.9-SA-NO_3	0.9 wt% Pd @ ECN, Pd-Precursor: $Pd(NH_3)_4(NO_3)_2$
ECN-Pd-1.3-SA-NO_3	1.3 wt% Pd @ ECN, Pd-Precursor: $Pd(NH_3)_4(NO_3)_2$
ECN-Pd-0.5-NP	0.5 wt% Pd nanoparticles @ ECN, Pd-Precursor: K_2PdCl_4
P4–Ru-0.4-SA	0.4 wt% Ru single-atoms @ P4, Ru–Precursor: (Dichloro(*p*-cymene)ruthenium(II))
P4–Ru-12.6	12.6 wt% Ru @ P4, Ru Precursor: (Dichloro(*p*-cymene) ruthenium(II))

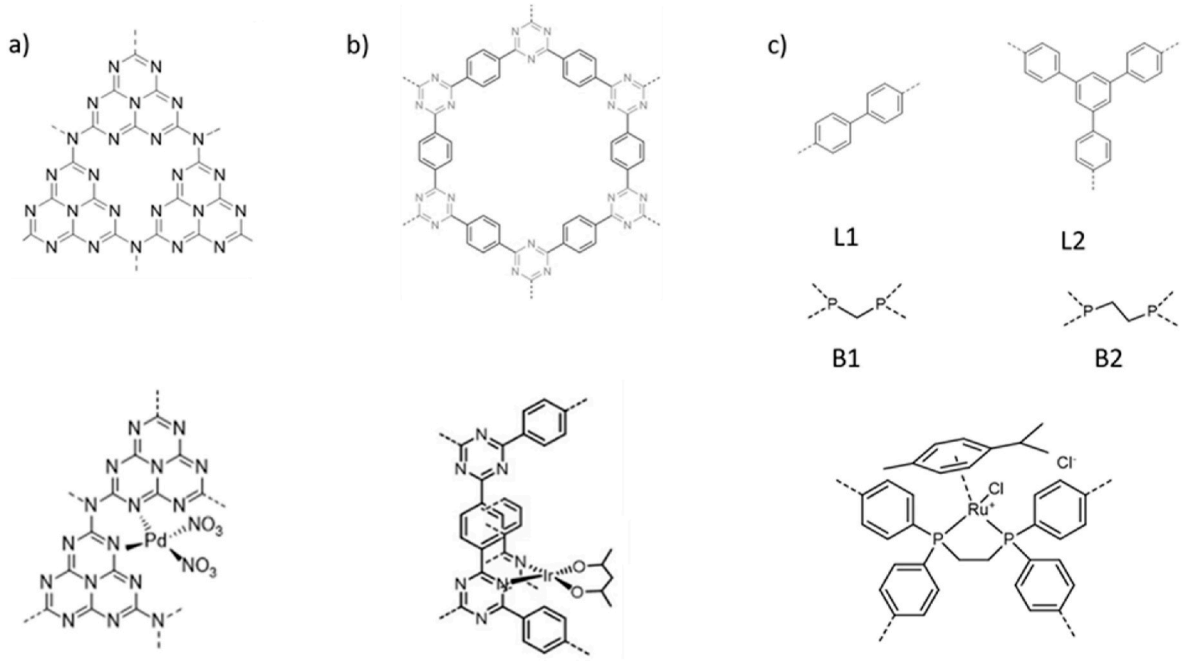

Fig. 1. Schematic structure units of the polymeric support materials exfoliated graphitic carbon nitride (ECN) (a), covalent triazine frameworks (CTF) (b) and polyphosphines (c) including a representation for a potential coordination environment of the atomically dispersed metal species. For the polyphosphines, L refers to linker while B refers to bridge. The repeating structure unit of each polyphosphine consists of one bridge and four linkers.

discussed support materials, their abbreviations and sample information.

The different support materials were loaded with varying amounts of different late transition metals to result in the catalyst samples. Table 2 contains the sample abbreviations for the catalyst samples used through this work, including sample information. The catalyst samples containing SA (single-atom) in their abbreviations are assumed to contain isolated metal sites, while NP (nanoparticle) describes a as-synthesized nanoparticle catalyst. In the work of Vennewald et al., Pd immobilized on ECN was tested as a catalyst for the hydrogenation of ethylene [14]. It was found that Pd in the catalyst is in oxidation state two and therefore has to have two X and two L ligands. If $Pd(NH_3)_4(NO_3)_2$ was used as a Pd precursor, NO_3^- was assumed as X ligand whereas when K_2PdCl_4 was used, Cl^- was assumed instead. Based on those two systems, in this work we refer to the samples ECN-Pd-0.5-SA-NO_3 and ECN-Pd-0.5-SA-Cl, respectively, each containing 0.5 wt% Pd. Additionally, a sample containing 0.5 wt% Pd nanoparticles was synthesized (ECN-Pd-0.5-NP). The catalytic activities of all catalysts were compared. It could be shown that ECN-Pd-0.5-NP was immediately active while both ECN-Pd-0.5-SA-NO_3 and ECN-Pd-0.5-SA-Cl only turned into active catalysts after being exposed to 100 °C in a specific gas atmosphere during a temperature program. Furthermore, ECN-Pd-0.5-NP functions as a reference for Pd–Pd pair correlations in the PDF analysis. In addition to the computational studies, the local and electronic structure of Pd in these samples have been analyzed via X-ray absorption spectroscopy (XAS) and *ex situ* X-ray photoelectron spectroscopy [52]. To validate the significance of small dPDF peaks, catalysts with higher Pd loading (0.9 and 1.3 wt%) were also analyzed. Those samples are named ECN-Pd-0.9-SA-NO_3 and ECN-Pd-1.3-SA-NO_3, respectively. Polyphosphine P4 was loaded with 0.4 wt% Ru, which is named P4–Ru-0.4-SA throughout this work. As a comparison P4 was also loaded with 12.6 wt% Ru as a reference for clear Ru-X pair correlations, which is abbreviated as P4–Ru-12.6.

The details on the materials synthesis are given in the supporting information.

3. X-ray total scattering and pair distribution function analysis

The aim of X-ray total scattering (XRTS) experiments is to extract local structure information from the sample, often by applying a subsequent pair distribution function (PDF) analysis. PDF analysis requires TS data that were acquired to high Q-values, where $\boldsymbol{Q = 4\pi\, sin(\theta)\,/\lambda}$ with good measurement statistics. In the equation, $\boldsymbol{\theta}$ is the scattering angle and $\boldsymbol{\lambda}$ is the wavelength of the X-ray radiation. While laboratory devices have been traditionally utilized and can provide sufficient quality data in various cases [53], the use of high-energy, high-flux synchrotron radiation with 2D data collection is recommended especially for weakly scattering systems and dilute species [54]. The significantly lower X-ray flux from laboratory anodes poses a huge challenge when studying components with very weak signals. The low scattering intensity of the target materials is due to several reasons, including the low scattering power of the elements in the polymer backbone (N, C, P), the low overall density of the material, the dilute concentration of the catalyst sites loaded into the support, and the overall disordered structuring of the support material. These issues typically result in a much higher ratio of background scattering from air and capillary material, and make the accurate extraction and normalization of the high-Q structure function far more challenging. The X-ray total scattering patterns for the support materials are given in Fig. S1. It is visible that only the ECN shows pronounced Bragg reflections while these are absent for the Z-CTF and the polyphosphine. This indicates that the Z-CTF and the polyphosphine lack a 3D lattice periodicity. Fig. 2 provides an illustrative example of the dominance of the scattering intensity of the support material in single-atom catalysts. The XRTS data of the pure ECN and the ECN-Pd-0.5-SA catalyst are compared. No indications for additional scattering intensities of the immobilized metal can be found. By comparison with ECN-Pd-0.5-NP [14] small additional

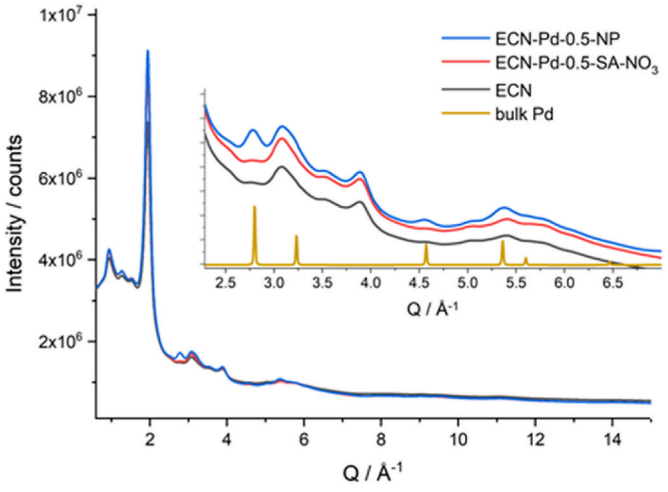

Fig. 2. X-ray total scattering data of the support material ECN (black), the ECN loaded with 0.5 wt% Pd single-atoms (red) and the ECN loaded with 0.5 wt% Pd nanoparticles (blue). The cutout shows a zoom into the Q-range between 2.3 and 7 $Å^{-1}$ containing Bragg reflections stemming from bulk Pd in ECN-Pd-0.5-NP.

reflections (e.g. at 2.8 $Å^{-1}$) indicating the presence of Pd crystallites can be seen. The simulation of the diffraction pattern is based on a Pd crystal structure obtained from the ICSD-database (ICSD-77885) [55].

The X-ray total scattering data of P4 before and after loading with 0.4 wt% Ru (P4–Ru-0.4-SA) are shown in Fig. S2 and are virtually indistinguishable.

For all single-atom systems studied, after impregnation with a metal precursor, the X-ray diffraction data show no clear difference compared to the unloaded polymer. This finding supports the assumption of highly dispersed metal sites in the different single-atom catalysts. This comparison highlights the necessity of being able to study minor differences in the local structure of single-atom catalysts. Atomic pair distribution function (PDF) analysis can be performed by Fourier transformation of total scattering data. Its development regarding the analysis of molecular materials has made great advances, especially in recent years. A detailed description of the data processing and underlying theories can be found elsewhere [28,56–58]. PDFGetX3 is a recommended data reduction package for extracting relevant information from the integrated X-ray total scattering data [59]. Correction for experimental aberration, removing residual, unwanted scattering contributions, normalization and Fourier transformation are included in its ad hoc methodology [60]. This results in a relative scaling and arbitrary absolute intensities of the PDF, which should be considered depending on the goal of the analysis.

Generally, a PDF analysis reveals direct structural information intuitively as it represents a weighted histogram of interatomic distances in real space. Therefore, insights such as the presence of particular bond distances, their distribution and probability, and extent of structural coherence can be extracted [28]. Determinations of structural coherences can be achieved by the analysis of the amplitude of the PDF signal, as evidenced in the plot. Fig. 3a shows the structural coherence of the different polymeric support materials. It can be seen that polyphosphines and CTFs show a similar coherence. However, the pair correlations in the Z-CTF remain sharper. This indicates a higher structural rigidity of the layers compared to the polyphosphines. The polyphosphines might have more conformational possibilities and therefore a broader distribution of interatomic distances resulting in broader PDF peaks. Only the PDF of ECN indicates extended coherence seen as an oscillation in the atomic density up to ~60 Å, which is due to the interlayer stacking. For a detailed PDF analysis of graphitic carbon nitride, the reader is directed to other publications [61–63].

The zoom-in to the higher r-range of the polyphosphines and the Z-

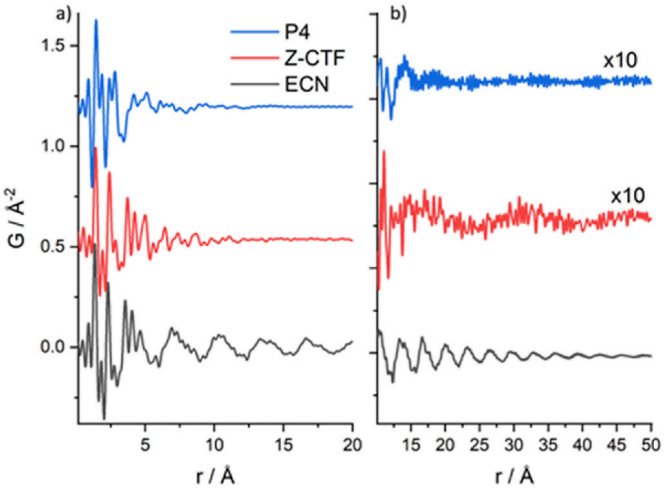

Fig. 3. PDFs of the polymeric support materials in a r-range between 0 and 20 Å (a) and between 13 and 50 Å (b). Curves are plotted with an offset.

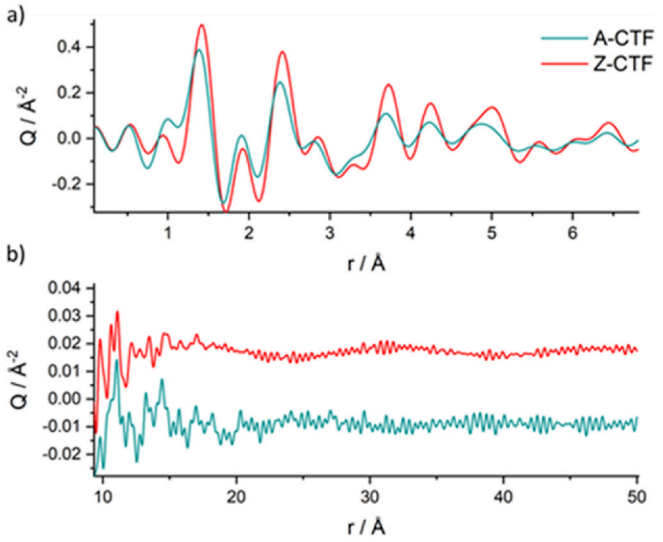

Fig. 4. PDFs of the differently synthesized CTFs. A-CTF represents a non-carbonized CTF that was synthesized via a low-T synthesis method while Z-CTF represents a carbonized CTF, which was synthesized at high temperatures. For better visualization, the PDFs are shown offset in b).

CTF in Fig. 3b shows slight oscillations in the PDF data of the Z-CTF. This may be indicative of the existence of an ordered porosity in the Z-CTF, which is not present in the polyphosphines. In all cases the well-defined PDF peaks at short distances are in good agreement with the structural motifs the polymers consist of such as benzene, triazine and 1,2-Bis (diphenylphosphino)ethan (DPPE). This can be confirmed by a comparison with the simulated PDFs based on crystallographic data of benzene (CCDC-1843297), triazine (CCDC- 1275718) [64] and DPPE (CCDC-2065417) extracted from the Cambridge Crystallographic Data Center CCDC (Fig. S3). The different compositions result in different frequencies of certain atom-pairs, so the peak positions observed in the low r-range PDF are modified accordingly. This allows to distinguish between C–N (1.36 Å) bond distances present in ECN, the C–C (1.45 Å) distance of the benzyl rings or C–P (1.87 Å) distances in the polyphosphine. The bond correlations for the Z-CTF structure that is composed of both triazine and benzyl are found in between. It is difficult to resolve contributions between, e.g., C–N versus C=C due to their overlapping distributions. Nevertheless, the overall width of the peak and often even peak asymmetry help to indicate changes due to varying contributions [65]. A feature at ~1.8 Å is also found in the PDF of ECN and Z-CTF despite an absence of C–P – this is a termination ripple due to the limitation in the Q-range (here $Q_{max} = 17$ Å^{-1}). A variation of the Q_{max} value allows to distinguish real pair correlations from termination ripples. In Fig. S3c the PDFs of the polymer building blocks were simulated at a Q_{max} of 100 Å^{-1}, eliminating potential termination ripples and confirming a C–P pair correlation at ~1.8 Å in DPPE which is absent for benzene and triazine.

Besides bond distance distributions, relative molecular rigidity, and interlayer stacking properties, structural refinements against the PDF can give further information about differences in structural coherence and relative ordered vs. disordered contents in semi-crystalline polymers. This was demonstrated for polyamides produced via different synthetic procedures [66]. Structural differences due to varying synthetic procedures can also be observed in the material class of the CTFs. Therefore, the PDFs of the carbonized Z-CTF and the non-carbonized A-CTF are compared in Fig. 4. Fig. 4a shows the short-r range PDFs of the CTFs and it can be seen that the first three real pair correlations are slightly shifted towards higher distances in the Z-CTF. This is due to the increased presence of benzyl rings compared to triazine rings in the carbonized CFT, i.e. more C–C bonds than C–N bonds. This is in agreement with the finding that a higher synthesis temperature leads to a loss of nitrogen (up to 10 wt%) in the CTF framework as it was shown by elemental analysis [22,44].

Considering the region between 3.5 Å and 5.5 Å, the pair correlations for the A-CTF appear broader and less defined. This indicates a higher degree of disorder and/or a broader distribution of the corresponding interatomic distances. A potential explanation would be that the Z-CTF shows a thermodynamically favored and therefore more defined local structure due to the high synthesis temperatures. The lower temperature synthesis of the A-CTF might result in the presence of different possible conformations in the short-range order. Fig. 4b shows the intermediate and long r-range of the two CTFs. Considering the range between 10 and 22 Å, the trend changes and the pair correlations of the A-CTF remain more defined. This might be due to the more ordered hexagonally packed layers in the A-CTF. However, local offsets between neighbouring layer have been directly shown in 2D COFs [67]. In a range between 23 and 50 Å broad low-wavelength oscillations in the PDF of the Z-CTF can be seen. As previously stated, this phenomenon may be attributed to the presence of a well-defined mesoporosity in the Z-CTF, which is not observed in the A-CTF. This is in line with the findings of Kuhn et al. who described the material as a polymer scaffold with well-defined mesoporosity and thus a very high surface area, which however does not exhibit regular arrangement [51]. Also in the material class of polyphosphines structural differences depending on the synthesis procedure can be observed by PDF analysis. P3 and P4 are examples for polyphosphines containing different linkers with different amounts of C–C bonds. The corresponding PDFs and detailed explanation can be found in Figs. S5 and S6.

4. Local structure analysis of single-atom catalysts via dPDF analysis

Similar to the case of the X-ray diffraction patterns, where the total signals are dominated by the support contribution, it can be very difficult to extract structural information from any immobilized metal species by assessment of the total PDF signals. Even for the ECN-Pd-NP sample, contributions of the nanoparticles are difficult to identify as potential pair correlations overlap with pair correlations related to the support (Fig. S7). A very useful application when it comes to the analysis of very dilute samples is the called difference atomic pair distribution function analysis (dPDF). The principle of subtracting all unwanted scattering contributions allows the isolation of tiny differences in scattering intensity enabling the extraction of pair correlations related to the component of interest only. Here, we measure the X-ray total scattering contribution of the unloaded support material and use it as background,

assuming that it represents the bulk of the single-atom catalyst except for the immobilized metal centers.

Among the samples analyzed, ECN-Pd-0.5-NP was the most promising to give a clear dPDF, as evidence for bulk Pd could already be found in the total scattering data in the form of small matching Bragg reflections (Fig. 2) [14]. Difference signals from even small nanoclusters embedded in microporous supports can often be extracted and quantitatively analyzed to determine both structuring and crystallite size distributions [68]. The Pd–Pd bond distances of the nanoparticles were successfully isolated and the respective dPDF fitted with a known fcc Pd structure (ICSD-77885) and a spherical nanoparticle model in Diffpy-CMI following Juhas et al. [69,70]. The dPDF fit of ECN-Pd-0.5-NP is shown in Fig. S8. The difference curve contains oscillation-like features. Such long wavelength oscillations in the difference curve hint at differences in interlayer correlations. One potential explanation could be that the presence of nanoparticles induces strain onto the layers for example by altering the interlayer connectivity.

To obtain a significant dPDF of the single-atom catalyst samples, it was essential to ensure that the quality of the data was of a high standard and to exercise caution during the data processing stage. The considerable impact of the data quality on the resulting dPDF is illustrated in Fig. 10, with a comprehensive account provided in the section on *Measurement and data processing considerations*. The dPDF of sample ECN-Pd-0.5-SA-NO_3 is shown in blue in Fig. 5 and is compared to the dPDFs of the higher loaded Pd catalyst samples ECN-Pd-0.9-SA-NO_3 and ECN-Pd-1.3-SA-NO_3, respectively. It can be seen hat the pair correlation at 2.02 Å increases with an increase in the loading of palladium. This confirms that the pair correlation correlates to Pd-X. The additional comparison with the dPDF of ECN-Pd-0.5-NP in Fig. 5 demonstrates the absence of Pd–Pd pair correlations in the single-atom catalyst samples. It indicates the successful isolation of the metal sites even at a Pd loading of 1.3 wt%.

In order to gain insights into the local bonding environment of single-atom catalysts, it is of significant value to corroborate the findings with a PDF analysis of reference materials. This allows to get an overview on possible bond distances related to differently coordinated Pd species and in different formal oxidation states. Fig. S9 shows the PDF fitting of reference samples K_2PdCl_4 (ICSD-27522) [71], K_2PdCl_6 (ICSD-73723) [72], PdO (ICSD-24692) [73], $Pd(NH_3)_4Cl_2$ (ICSD-15990) [74], and Pd-phen-Cl_2 (CCDC-766662) [75] including a visualization of the crystal structures. It is possible to evaluate and compare how the positions and intensities of the pair correlations associated with Pd are affected. More details about the PDF analysis of the reference materials is provided in the SI. The PDF analysis of the reference materials revealed that the Pd-X pair correlation at 2.02 Å in the dPDFs of the single-atom catalysts can be attributed to either Pd–N or Pd–O.

In order to ascertain the impact of the Pd precursor on the local structure of the single-atom samples, the dPDFs of ECN-Pd-0.5-SA-NO_3 and ECN-Pd-0.5-SA-Cl were subjected to a comparative analysis, as illustrated in Fig. 6. This indicates that the Pd-X bond distances and, consequently, the coordination environments are different depending on the choice of the Pd precursor. A peak at 2.3 Å can be identified in the dPDF of ECN-Pd-0.5-SA-Cl, which can be attributed to Pd–Cl based on a comparison with the PDFs of the reference structures.

Furthermore, computational studies offer the possibility to gain complementary structural insights especially for complex and dilute samples. They are not a guarantee of a particular real structure, but they can exclude certain conformations. In the work of Vennewald et al., they calculated binding energies for Pd core levels and the Gibbs energy of formation in accordance with ECN-Pd-0.5-SA-NO_3 and ECN-Pd-0.5-SA-Cl [14]. The DFT-optimized structures for these two cases are shown in Fig. S10. On the one hand, the structure models obtained from such calculations can be used to access bond distances in certain coordination environments. The bond distances are in line with the values extracted from the PDF analysis of the reference materials. On the other hand, they can be in theory used to simulate PDFs and dPDFs. Those can then be compared and fitted to the experimental data [33]. Fig. S11 shows the theoretical dPDFs based on the DFT-optimized model structures. It can be seen that for both systems, there is a good agreement between the first nearest neighbor atomic pair correlation of the simulated dPDFs and the experimental data. Based on these results it can be concluded that the first coordination shells of sample ECN-Pd-0.5-SA-NO_3 and ECN-Pd-0.5-SA-Cl_2 contain Pd–N and/or Pd–O pair correlations and Pd–Cl pair correlations, respectively. However, such a comparison is only reasonable if the proposed structure comes close to a realistic bonding environment and should be backed up with experimental data. However, it should be kept in mind that the proposed structures do not properly account for a layered material or the energetics of a condensed bulk structure.

The dPDF analysis was also applied to the polyphosphine based single-atom catalyst P4–Ru-0.4-SA that was found to be active in CO_2 hydrogenation [45–47]. Again, a sample with higher loading

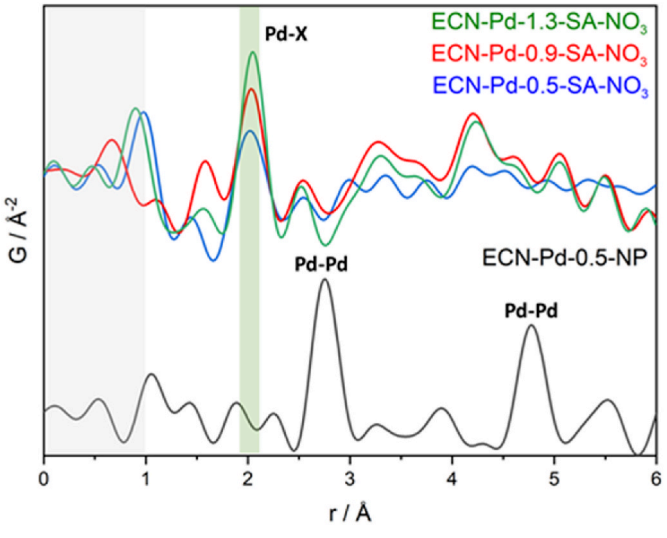

Fig. 5. dPDF analysis of the ECN-Pd-SA samples containing 0.5 (blue), 0.9 (red) and 1.3 (green) wt.% Pd loading. The figure includes the dPDF of the ECN-Pd-0.5-NP sample showing Pd–Pd pair correlations (shown with offset). Pair correlations in the very small r-range (<1 Å) are considered unreliable based on XRTS data and are marked by grey shading.

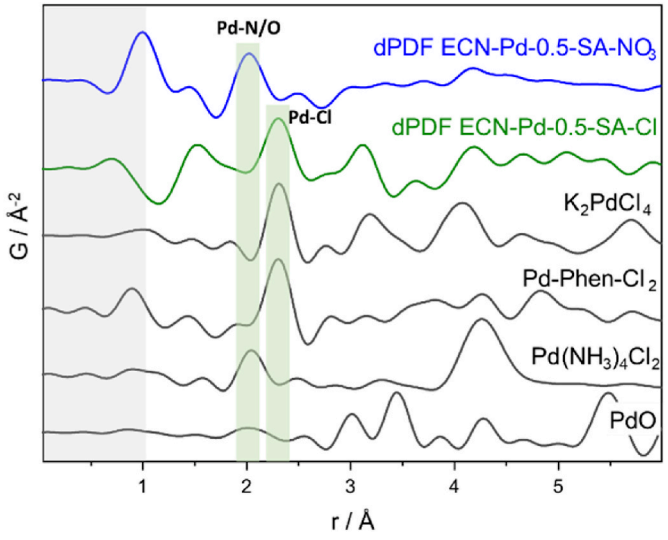

Fig. 6. A comparison of dPDFs of ECN-Pd-0.5-SA samples synthesized with different precursors and PDFs of reference materials (shown in black). The data were normalized and plotted with an offset.

(P4–Ru-12.6) was analyzed for comparison to obtain a Ru-X signal with high intensity. Furthermore, PDF analysis was performed for [Ru(dppe)) p-cym)Cl]Cl (CCDC-254639) which is a representative material for the expected coordination environment of the immobilized Ru in P4–Ru-0.4-SA. To investigate the potential presence of Ru clusters or nanoparticles, a theoretical PDF based on a bulk Ru structure (ICSD-40354) [76] was simulated to provide Ru–Ru pair correlations for comparison. The two experimental dPDFs are compared with the PDF of the reference structure, the PDF of the *p*-cymene ligand and the simulated PDF for bulk Ru in Fig. 7.

The dPDF of P4–Ru-12.6 shows a good agreement with the PDF of the reference structure and suggests a successful metal loading and maintenance of isolated Ru sites. It can be seen that the main pair correlation of the reference structure at 2.3 Å, which originates from either Ru–P or Ru–Cl, matches the most dominant peak in the dPDF. In this system (dichloro(*p*-cymene)ruthenium(II)) was used as a Ru precursor. After the impregnation with the precursor, the structure should not only contain additional Ru–P and Ru–Cl bonds but also C═C pair correlations due to the additional *p*-cymene ligand. In fact, a pair correlation at 1.4 Å, matching a C═C bond distance, can also be clearly observed.

In comparison, the dPDF of P4–Ru-0.4-SA shows an overall much lower magnitude difference indicative of the much lower Ru loading content. Since the signal is more than an order of magnitude less than for the dPDF of P4–Ru-12.6, as expected, we must be careful in assigning feature here, as they are of a similar magnitude as the termination effects in the data. Nevertheless, there do appear to be similar features at approximately the distance of C═C and Ru–P/Cl. However the relative intensity of C═C peak is much higher in this case. This could suggest that there is excess addition. There also appears to be increased intensity at a slightly higher distance from the peak assigned to Ru–P/Cl. This distance could be assigned to metallic Ru–Ru, however there is no evidence of metallic Ru from XPS analysis conducted on both samples [48]. It is also not expected to have increased Ru–Ru with lower wt.% of Ru. Alternatively, this peak could also coincide with the second nearest neighbor distance in the ligand, which is consistent with the increased relative intensity of C═C peak. We tested the reliability of the dPDF

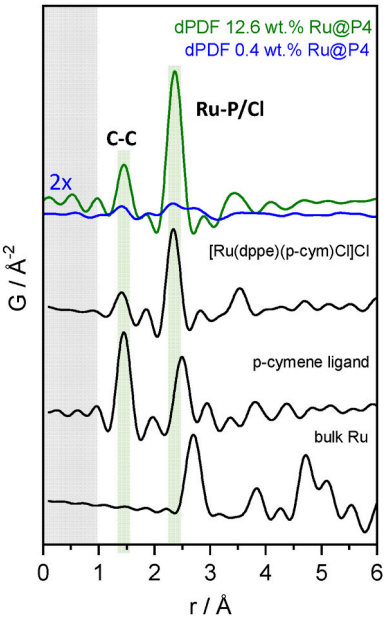

Fig. 7. The coloured lines show the dPDF analysis of P4–Ru-0.4-SA (blue) and P4–Ru-12.6 (green) which are compared with the PDFs of the reference structure [Ru(dppe)(*p*-cym)Cl]Cl, the PDF of the *p*-cymene ligand and the simulated PDF of bulk ruthenium. The dPDF of P4–Ru-0.4-SA is presented here at a 2× magnification in order to enhance its visibility. The data of the reference materials were normalized and plotted with an offset.

signals by processing the data with varying Q_{max} values as shown in Fig. S12. It can be seen that the dPDF of P4–Ru-0.4-SA does appear to be robust. However given the order of magnitude decrease in signal compared to P4–Ru-12.6, the effects of other potential structural changes not corresponding to the presence of Ru-complex, and no metallic Ru observed by XPS, we should take care not to over-analyze this feature. The correspondence of the C═C and Ru–P/Cl features suggests that the limit of detection does appear to be at least or below 0.4 wt%, but the structural interpretation at this loading level remains inconclusive. A more extensive discussion on the limitations of dPDF analysis is given in section 5.

5. Limitations of the difference pair distribution function analysis

What has to be acknowledged is the general assumption of the dPDF method that the immobilization of the metal species causes a negligible change in the structure of the support material. This means that if the structure of the support is only slightly modified upon the metal impregnation process, these differences will not be subtracted during the background optimization. Potential differences could be conformational, chemical or other. Consequently, extra peaks will be found in the dPDF, which cannot be solely explained by Pd-dPDF models. Similarly, subtle differences in the support materials structure due to slight differences during the synthesis of different batches can also cause such effects. It is therefore essential to ensure that the support material, which is loaded with the metal species, is from the same experimental batch as the pure support material for subsequent XRTS measurements with the aim of performing a dPDF analysis. It can be seen in Fig. 5 that the samples containing 0.9 and 1.3 wt % Pd shows additional dPDF features (between 2.8 and 5.0 Å) compared with the 0.5 wt % sample. Differences in metal loading could lead to density differences between the support material and the higher loaded catalyst samples. While we assume this density difference to be negligible between the support and the low loaded catalyst sample it can not be excluded for the samples containing increased load of Pd. Slight alterations in the chemistry, attributable to increased Pd content, can alter the packing behaviour and therefore the packing density of the material within the capillary. The packing density has been demonstrated to influence the signal-to-noise ratio of specific measurements, thereby generating termination ripples and, consequently, potential additional features. Even minor discrepancies in beam absorption between the catalyst sample, the corresponding unloaded support material, and the background constitute a significant challenge to the precise subtraction of the latter. Additionally, it is also conceivable that the structure of the support material is altered with increasing metal loading. The same applies to the dPDF of ECN-Pd-0.5-SA-Cl, which shows additional peaks (at 1.6 Å and 3.1 Å, Fig. 6) that could not be assigned to any explainable binding environment of palladium. Due to the metal-support interaction, the presence of a Pd–N bond correlation would be expected in the dPDF of the single-atom catalysts independent of the precursor used. However, no distinct peak was detected in the dPDF of ECN-Pd-0.5-SA-Cl. This effect was also visible during the PDF analysis of the reference materials. In Pd-phen-Cl_2, the Pd atom is coordinated to two pyridinic nitrogen atoms and two Cl-ligands. Nevertheless, the dPDF shows only one pair correlation at 2.29 Å whereas the contribution from Pd–N (2.03 Å) bonds cannot be resolved (Fig. S9). This might be due to the higher overall scattering intensity of the Pd–Cl bond. Distinguishing between termination ripples and true dPDF signals is a challenge when interpreting the catalysts data. It is important to note that the termination ripples are influenced by a number of factors: 1. The Q_{max}, the relative amount of coherent scattering measured at Q_{max} (a function of the scattering power of the elements in the sample and, potentially, their atomic displacement factors), and the signal-to-noise ratio of the specific measurement. The assessment of truncation errors typically involves the comparison of data across a range of Q_{max} values. It is notable that

structural signal is relatively impervious to minor fluctuations in Q_{max}. However, termination ripples demonstrate a pronounced sensitivity, exhibiting substantial variation in response to changes in Q_{max}. The presence of significant fluctuations in the structural signal as a function of Q_{max} is indicative of termination ripples or, at the very least, of their strong influence on the signal. In the event of a robust structure model and high-quality data being available, the termination effect can be incorporated into the real-space refinement process and reproduced with a reasonable degree of accuracy. However, given the questionable validity of the model in this instance, the termination ripple assessment cannot be as precise. This underscores the importance of reference materials, such as Pd references or comparisons with higher loading, in ensuring the reliability of the findings.

6. Local structure analysis of a Pd single-atom catalyst under reaction conditions

In the previous section it was illustrated that it is possible to extract local structure information from single-atom catalysts via X-ray total scattering and dPDF analysis. That the static ex situ measurements proved invaluable in facilitating discussion on optimized sample preparation and measurement conditions, as well as in demonstrating the applicability of the method for the analysis of the materials discussed in the context of this research project is later discussed in section 7. Nevertheless, it has been demonstrated in numerous studies that it is of crucial importance to monitor the structural evolution of active sites under reaction conditions in order to establish the appropriate structure-property relationships [19]. Especially, the avoidance of oxygen exposure in order to exclude misleading conclusions was highlighted.

It has been shown in the work of Vennewald et al. that the Pd single-atom catalyst on ECN showed a dynamic behaviour in the hydrogenation of ethylene. Distinct activation profiles were observed for the single-atom (ECN-Pd-0.5-SA-NO_3) and the nanoparticle (ECN-Pd-0.5-NP) catalyst [14]. The catalyst was characterized in consideration of aberration-corrected scanning transmission electron microscopy, X-ray photoelectron spectroscopy and X-ray absorption spectroscopy. It was concluded that an initially inactive single-atom catalyst transforms into an active material at 100 °C in a gas atmosphere containing each 2 vol % ethylene and H_2 in Argon due to the *in situ* formation of small Pd clusters. Here, we performed *in situ* X-ray total scattering experiments under reaction conditions to follow the local structure changes of ECN-Pd-0.5-SA-NO_3, which have initiated the reported activity at 100 °C. Special attention was paid to the observation of Pd–Pd atomic pair correlations in the dPDFs over the course of the reaction. The measurements were carried out at P02.1, PETRA III, DESY, with a dedicated PDF flow cell that allows to expose the sample to different gas atmospheres and temperatures (see Fig. S13). The obtained dPDFs of the *in situ* experiments are still overlaid by unresolved background scattering contributions due to the limitations of the data quality, and thus are not comparable with the clearer *ex situ* data discussed in the previous section. Nevertheless, some systematic changes could be observed. To ensure the accuracy of the background subtraction process, the ECN support was subjected to the same reaction conditions. Consequently, it can be assumed that the observed systematic changes are due to changes in the immobilized metal species over time.

Fig. 8 a) and b) show the normalized *in situ* dPDFs of Pd-0.5-SA-NO_3 over the course of reaction. Fig. 8 a) shows a comparison of dPDFs obtained after 15 min in each reaction step while Fig. 8 b) compares the dPDFs after a holding time of 120 min at each temperature step. It is known from the *ex situ* study shown in Fig. 5 that the dPDF of the Pd nanoparticle catalyst ECN-Pd-0.5-NP shows two clear peaks at 2.75 and 4.78 Å representing characteristic Pd–Pd bond distances. These areas are highlighted in green in Fig. 8. After a holding time of 15 min it can be seen in Fig. 8 b) that especially the dPDFs collected at 200 and 300 °C show increasing intensity between 2.6 and 2.8 Å and at 4.8 Å. This trend gets slightly more pronounced after a holding time of 120 min especially

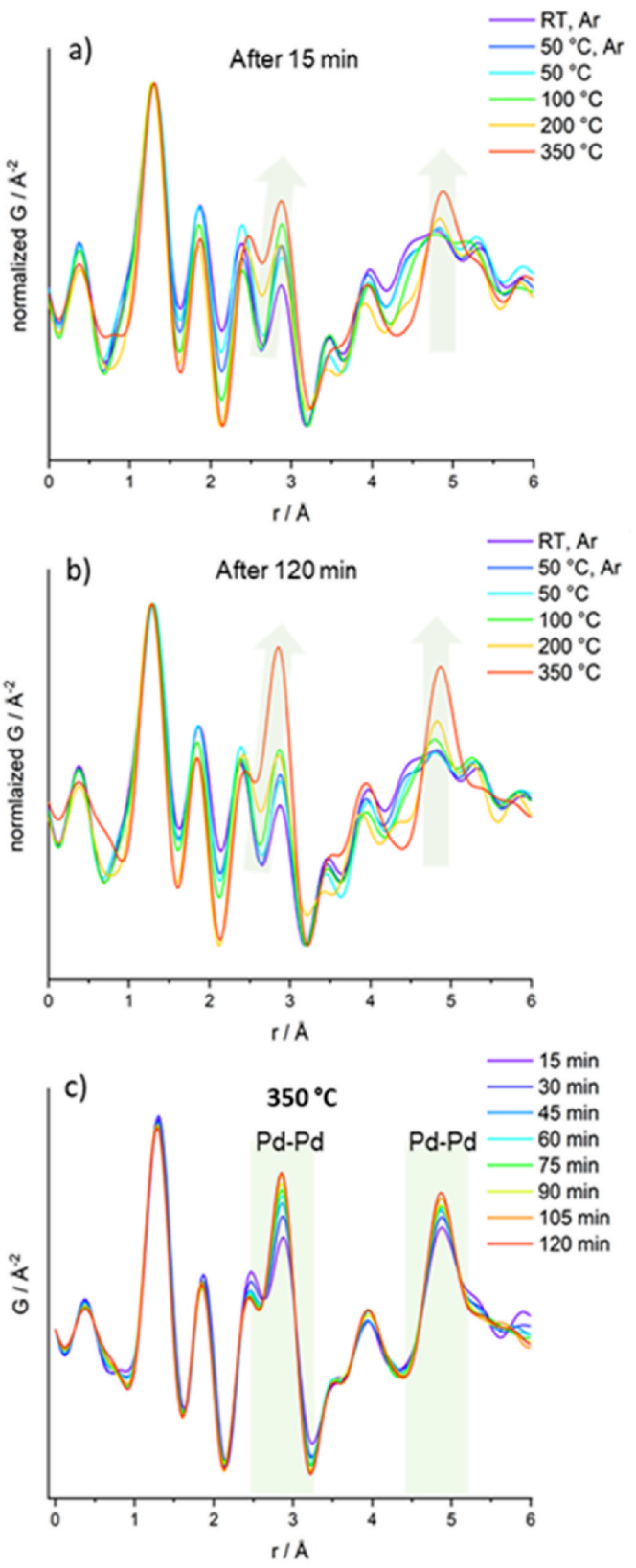

Fig. 8. In situ dPDFs of ECN-Pd-0.5-SA-NO_3 at RT, at 50 °C in Ar and at 50 °C, 100 °C, 200 °C and 350 °C in an atmosphere containing each 2 vol% H_2 and ethylene in argon after an reaction time of a) 15 min and b) after a total holding time of 120 min. Fig. 8c) shows the *in situ* dPDFs at 350 °C over the 120 min holding time in 15 min steps. Areas with noteworthy changes are marked in light green.

at 350 °C where the formation of Pd–Pd pair correlations can be clearly detected. Fig. 8 c) shows the evolution of the sample's local structure over the 120 min holding time at 350 °C in 15 min intervals. It can be seen that the peaks, which are associated with pair correlations of bulk Pd systematically grow with increasing holding time. This confirms the steady growth of the formed Pd nanoparticles at 350 °C with time and is proof of the consistency of the obtained data despite the difficult experimental conditions. After cooling to room temperature, the Pd–Pd pair correlations remain present. Nevertheless, the lack of sufficient data quality and the extremely low scattering contribution of the metal species precludes the drawing of any conclusions based on this *in situ* dPDF analysis alone.

Complementary to the *in situ* dPDF analysis, the electronic structure of Pd on the surface of the catalyst was studied via quasi *in situ* X-ray photoelectron spectroscopy (XPS). Usually, XPS measurements are performed ex situ before and after catalysis. However, the special experimental setup allows to apply reaction conditions to the sample without exposing the sample to air between the XPS measurements. It can be seen in Fig. 9 that the as prepared single-atom catalyst shows two distinct Pd species with binding energies (BE) of the Pd $3d_{5/2}$ photopeaks at 338.1 eV (i) and 336.3 eV (ii) related to different Pd^{2+} species. Afterwards the sample was successively exposed to temperatures of 50 °C, 100 °C, 200° and 350 °C in an atmosphere containing each 2 vol% H_2 and ethylene in Ar. Measurements were performed after each temperature step and a holding time of 2 h resembling the conditions of the *in situ* X-ray total scattering experiments. As shown in Fig. 9, the rise of the temperature to 50 °C in a pure Ar atmosphere and the subsequent change to the reductive atmosphere at the same temperature do not affect the amount or the photoelectron peak position of the Pd species. A change of the electronic structure of Pd upon the change of the gas mixture to a reductive atmosphere could not be observed. However, the two mentioned steps lead to a slight decrease in relative areas of Pd^{2+} (i) and an increase of Pd^{2+} (ii) as shown in Table 3. This might be due to a loss of oxygen/water as the sample was treated 4 h at 50 °C. Species Pd^{2+} (ii) increases further when the sample is exposed to 100 °C. In addition, the appearance of another Pd species at lower binding energy (335.0 eV) could be detected. This binding energy is in line with values reported in literature for metallic Pd [77].

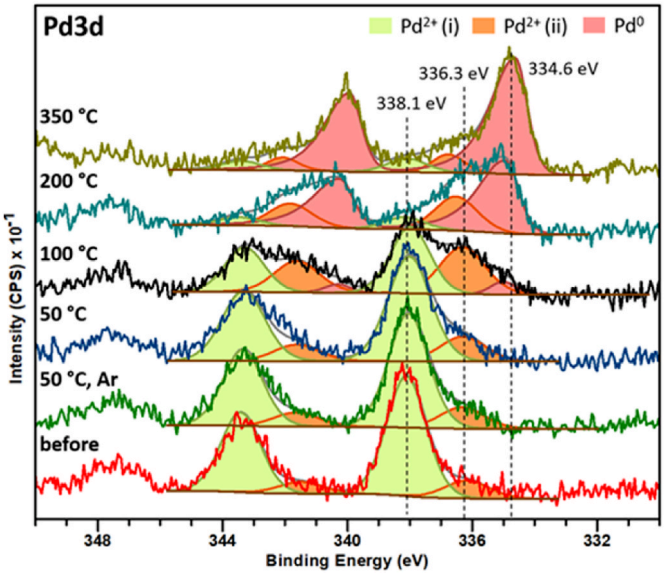

Fig. 9. Quasi *in situ* XPS spectra of sample ECN-Pd-0.5-SA-NO_3. At 100 °C the appearance of a third species could be detected, lying in the range of metallic Pd. With increasing temperature the binding energy of this species shifts to lower binding energies, indicating the growth of the formed nanoparticles. Spectra are shown offset.

When the temperature was further increased to 200 and 350 °C the peak intensity of the Pd^0 species increases while the Pd^{2+} species further decrease. At 350 °C, the relative peak area of the metallic Pd species dominates the Pd3d spectrum with 80.7 %. The peak position shifts to lower binding energies (334.6 eV) indicating a further increase of the electron density of Pd and therefore a growth of the formed Pd clusters/nanoparticles with temperature [78]. This observation is in line with the finding of the *in situ* dPDF analysis where Pd–Pd pair correlations could be identified at 350 °C. The results of this experiment support the assumption of Vennewald et al. that the emergence of catalytic activity of this catalyst at 100 °C coincides with the formation of small Pd clusters [14]. A change in the bonding state of Pd is also confirmed by considering the valence region at each temperature step shown in Fig. S14 [79].

It is challenging to make more specific statements on the nature of the two Pd species due to the presence of multiple functional groups and defects on the surface of the disordered support material. According to M. Vennewald, the most likely explanation is that the species result from different coordination environments based on the support. The observations made during the transition process of the quasi *in situ* treatment may be indicative of ligand exchange or removal, a phenomenon that is influenced by gas atmosphere and temperature changes. From 100 °C onwards, an increase in electron density is observed in Pd, attributable to an increase in the species at lower BE and the formation of a new metallic one at even lower BE. One potential explanation for this phenomenon might be the onset of NP or cluster formation, i.e. dimers or trimers, which begins to contribute in that BE range.

Resuming what has been mentioned earlier in this section, the avoidance of oxygen exposure by carrying out quasi *in situ* XPS measurements was decisive for the detection of the small Pd^0 species at 100 °C. The experiments confirm the hypothesis of Vennewald et al. that ultra-small Pd nanoparticles are the catalytically active species. This important result would not have been accessible by standard ex situ XPS measurements only. This study again highlights the importance of *in situ* characterization of heterogeneous catalyst in order to being able to draw the right scientific conclusions.

In comparison with the dPDF analysis of the sample ECN-Pd-0.5-SA-NO_3 where an average bulk local structure analysis cannot distinguish between Pd–N or Pd–O bond distances due to too large similarity, the XPS measurements can detect two electronically distinct Pd species on the surface of the catalyst. However, both techniques show no indications for metallic Pd in the initial SA catalyst but a dynamic behaviour indicating the formation of Pd–Pd pair correlations and the appearance of more electron rich Pd nanoparticles starting from 100 °C.

7. Measurement and data processing considerations

Throughout this research, we encountered several obstacles making the extraction of pair correlations related to the immobilized metal species in single-atom catalysts with low loadings and based on polymeric supports challenging. Therefore, we would like to systematically guide the reader through considerations with respect to preparing and performing the measurements. Furthermore, it will be explained according to which considerations the data were subsequently processed. It was found that X-ray total scattering data with optimized quality i.e. high signal-to-noise ratio at increased Q-range are crucial especially when aiming for subsequent dPDF analysis. As mentioned above, the low X-ray flux of laboratory diffractometers limits the analysis of samples with low scattering intensities. Consequently, performing the X-ray total scattering experiments at synchrotron facilities is of great importance. However, the access to synchrotron radiation alone does not automatically guarantee the generation of useful data. In order to extract minor but important scattering contributions it is necessary to reduce unwanted scattering contributions for instance from air or sample capillaries. It is also important to increase the counting statistics, improve the signal-to-noise ratio, and perform an accurate and

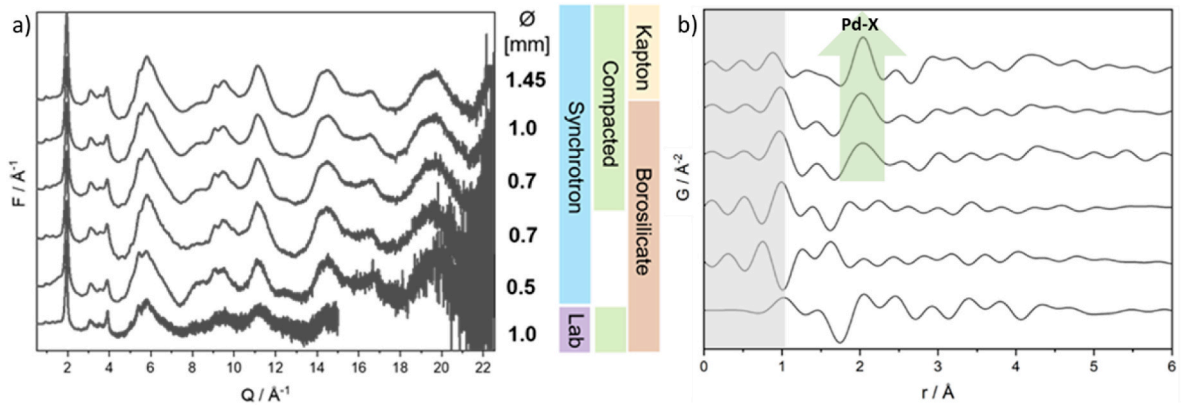

Fig. 10. a) Reduced total scattering structure functions of exfoliated graphitic carbon nitride depending on the capillary inner diameter, capillary filling and capillary material in a synchrotron X-ray total scattering experiment. b) dPDFs of sample ECN-Pd-0.5-SA-NO_3 depending on the data quality of the collected XRTS measurements as shown in a). A Pd-X pair correlation in the dPDFs appears more distinct with increasing signal-to-noise ratio of the underlying reduced total scattering structure functions as indicated by the green arrow. Data were normalized for easier comparison and are shown offset.

Table 3
Peak areas of Pd species relative to the total area of the $Pd3d_{5/2}$ signal for the quasi *in situ* XPS experiment on sample ECN-Pd-0.5-SA-NO_3.

	Area Pd^{2+} (i) [%]	Area Pd^{2+} (ii) [%]	Area Pd^{0} [%]
before	85.7	14.3	/
50 °C, Ar (pretreatment)	82.7	17.3	/
50 °C	80.0	20.0	/
100 °C	51.5	42.0	6.5
200 °C	12.1	29.8	58.1
350 °C	9.5	9.8	80.7

systematic background subtraction with validation of the resulting signals by plausible structural models.

7.1. Reducing air scattering

All experiments were performed at the Powder Diffraction and Total Scattering Beamline P02.1, PETRA III, DESY in Hamburg. In order to minimize air scattering, the beamline is equipped with a lead tube surrounding the incoming X-ray beam, which can be placed close to the sample. To reduce air scattering after the sample, the beam stop is moved as close to the sample as the setup allows. However, this limits the Q-range covered on the low-Q side of the data, and care must be taken to ensure that this does not truncate data containing structurally important information.

7.2. Increasing counting statistics

Counting statistics is an additional factor to improve data quality. At synchrotron sources, there are different measurement setups for X-ray total scattering experiments available with respect to the position of the area detector. Collecting full Debye scattering rings allows full azimuthal integration and thus maximizing the cross section of the Ewald sphere collected at once. However, this limits the maximum possible magnitude of the scattering vector, (Q_{max}) in the present case, which affects the resulting real space resolution. While not explored here, this can be mitigated with using higher X-ray energies. This reduces the resulting Q-resolution, but is generally not an issue when analyzing PDF data only over the first few angstroms. Oftentimes, the detector is instead placed such that the scattered beam is measured with only one quadrant of the detector. Thus, only one quarter of the full Debye rings is collected enabling data collection up to larger *Q*-values. However, this is at the expense of reduced data statistics as the azimuthal integration is limited to a quarter of the Debye ring. Also, this setup can exacerbate artefacts related to imperfect flat-field correction between different detector modules. High Q_{max} values are generally less critical for soft materials and low-Z systems because the damping of the X-ray form factors and larger Debye-Waller factor both lead to a reduction of coherent scattering signals at high Q- values that may either be insignificant or pragmatically inaccessible. For the materials analyzed in the framework of this study, the detector was placed in favor of increased data statistics.

Attention has been also paid to the data acquisition time of both the single-atom catalysts as well as the corresponding backgrounds, i.e. the empty capillary and the support material. Data were collected over periods of 30 min and then compared after summation at different time intervals. No significant difference could be observed by comparing resulting PDF or the dPDF after 15 and 30 min indicating that 15 min data acquisition time is sufficient. Nevertheless, this clearly depends on the analyzed materials and should be checked individually. It should be noted that the laboratory-based measurement shown in Fig. 10 took ~2.5 days to achieve the given data quality. It is also important to rotate the samples during the measurements to optimise orientation averaging and to avoid the effects of material coarseness/preferred orientation.

7.3. Increasing the sample volume

A major improvement on the signal-to-noise ratio for this specific class of materials was obtained by using capillaries with wider diameter as that increases the amount of sample that is hit by the beam and therefore the overall scattering intensity. This effect can be magnified by additionally packing the samples as tightly as possible. This was achieved by manually compacting the powder in the capillary with a straight metal wire slightly smaller than the capillary. It is important to remember that the amount of sample required to fill a larger diameter capillary will increase. Furthermore, one can also consider the capillary material. Typically, borosilicate capillaries are used for *ex situ* X-ray total scattering experiments. Using Kapton capillaries is a nice alternative for the measurement of weakly scattering materials as their own scattering contribution is lower in comparison to borosilicate glass capillaries. However, the usage of Kapton capillaries was carefully considered for the analysis of amorphous polymers as it contains long range ordering compared to borosilicate glass and has carbon bond correlations that overlap with the sample contributions. Nevertheless, errors from an imperfect background subtraction are small, especially with larger capillary diameters. Fig. 10a) shows the reduced total scattering structure functions of pure ECN that was measured (i) in capillaries with different inner diameters, (ii) with and without manually compacting the powder within the capillary, (iii) in a borosilicate glass and a Kapton capillary and (iv) based on laboratory and synchrotron X-

ray sources.

The Fourier transform of the TS data from beamline P02.1 shown in Fig. 10 was performed with the maximum magnitude of the scattering vector (Q_{max} 22.5 $Å^{-1}$) that could be achieved with the given measurement setup. As the size of the capillary increases, the signal-to-noise ratio increases strongly. In particular, the compaction of the powder within the capillary leads to improved data quality. Fig. 10 illustrates that the data which were collected in 1.45 mm Kapton capillaries and in 1.0 mm borosilicate glass capillaries have a comparable signal-to-noise ratio. Given that the sample amount was limited, the material preparation strategy was set to utilize 1.0 mm borosilicate glass capillaries and manually compacting the powder.

A Q_{max} value of 16.5 $Å^{-1}$ was considered appropriate for the Fourier transformation of the TS data in order to exclude data with a decreased signal-to-noise ratio. The resulting PDFs can be seen in Fig. S15. In fact, the influence of the improved signal-to-noise ratio due to powder compaction and increase of capillary diameter seems negligible on the resulting absolute PDFs. However, it could be shown that the dPDFs strongly depend on the data quality and therefore the optimized sample preparation as illustrated in Fig. 10b). It could be shown that powder compaction is the most important factor in obtaining reliable dPDFs. For the compacted samples, the increased capillary diameter leads to an improved dPDF signal i.e., decreased noise and sharper features. Based on the results of the optimized capillary preparation, a 1.0 mm compacted borosilicate glass capillary was measured with a laboratory diffractometer and Mo-Kα_1 radiation. The obtained F(Q) is compared to the synchrotron-based data in Fig. 10. Even though the measurement with the laboratory diffractometer allows only a Q_{max} of ~15 $Å^{-1}$, the features of the scattering pattern at low Q-values are comparable with the synchrotron data. The signal-to-noise ratio, however, is lower even at low Q-values. The laboratory-based dPDF of the sample ECN-Pd-0.5-SA-NO_3 is shown in Fig. 10 (bottom). The dPDF result was ambiguous even at lower Q_{max} values (Fig. S16), highlighting the preference for synchrotron radiation and large 2D area detectors for a reliable dPDF analysis of such dilute systems.

Fig. S17 shows the F(Q) of the carbonized Z- CTF and the non-carbonized A- CTF. The carbonized CTFs allow a better data quality i.e. better signal-to-noise ratio with increasing Q-value. This observation was made for both synchrotron as well as lab-based total scattering data. A potential explanation could be the higher bulk density of the Z-CTF compared with the A-CTF [80] leading to a denser packing of the material within the capillaries and therefore a better signal-to-noise ratio with increasing Q. Differences in structural flexibility and dynamics might also play a role. In the very low-Q range, two relatively sharp peaks can be found in the A-CTF while signals seem to become broadened and less distinct compared to the Z-CTF with increasing Q. However, analyzing small differences in the PDFs based on data with differing data quality needs to be done with caution. Very high scattering intensities of crystalline materials bear the risk of causing trapped states in CCD detectors that can remain and create peaks in subsequent measurements, especially if the following sample is weakly scattering [81]. Therefore, an appropriate cooling of the detector and sufficient "cleaning" steps in between longer measurements are crucial. Additionally, this should be considered when setting up an experimental plan. In order to prevent potential trapped states in the detector, amorphous and weakly scattering materials should be measured before the crystalline ones.

7.4. Background subtraction

The most important part of data processing for the dPDF analysis of very dilute samples is accurate background subtraction. The term 'processing' is used to denote the process of data reduction from TS data to PDF data. This process involves the correction, normalization and Fourier transformation of the integrated data to the PDFs. PDFgetX3 was used for to correct, normalize and Fourier transform the F(Q) function to access the PDFs. Intuitively, the X-ray total scattering data of the unloaded support materials were specified as the background in the configuration files for the Fourier transformation of the single-atom catalyst data. Even at 60 keV, very small differences in beam absorption between the measurements of background, reference, and target sample mean that multi-background optimization is needed to extract the weak sample signals as well as possible. The benefit of PDFgetX3 is also that the polynomial correction further accounts for minute deviations in the high angle behavior. While PDFgetX3 offers the functionality of multiple-background subtraction, hand optimization of multiple backgrounds is tedious, inaccurate, prone to user bias, and not easily reproducible.

For this study, a Python script was used which was developed to subtract multiple background contributions in real space by optimizing the scale factors for each component to minimize the least squares residual. The idea behind this is that the signals in the background should not significantly correlate with the dPDF signal. Fig. S18 shows the result of the fit including the PDF data of the catalyst sample, the PDFs of the backgrounds used and the resulting difference curve. The figure illustrates two important findings. First, the catalyst sample is clearly dominated by contributions from the ECN support. Second, the resulting difference curve is marginal. Only significant magnification allows to identify a potential pair-correlation peak at 2.02 Å. As the subtraction was performed in real space, the prior Fourier transformation of all data sets was conducted without considering any background file. For the data processing the same chemical composition was assumed for the expected immobilized metal species e.g. N_2O_6Pd. It is advisable to process the background PDF with the same final composition as the sample data. The rationale behind this is that when the F(Q) function is generated from I(Q), it is used to correct for the scattering cross section of the constituent elements. Consequently, it is necessary to employ a consistent composition to prevent systematic discrepancies in the resulting PDFs (and, by extension, the resulting dPDFs).

7.5. Specific considerations for in situ measurements

In comparison with the static *ex situ* measurements where the sample preparation and measurement conditions could be systematically optimized in order to increase the decisive data quality, the *in situ* measurements are influenced by many more factors. The measurements were performed in a dedicated flow cell in order to expose the powder to different gas atmospheres (see Fig. S12). Accordingly, this required the use of capillaries that are open on both sides. At the same time, the capillaries need to have a certain stability to guarantee a gas-tight fixation to the cell. In that respect we used borosilicate glass capillaries with a diameter of 1 mm and a wall thickness of 0.1 mm. Correspondingly, compared to the *ex situ* measurements, the contribution of scattering from the borosilicate glass is higher by a factor of 10. This makes the complex background subtraction even more challenging. Further adding to additional background contributions, the setup contains a heat blower located below the capillary to reach the desired temperatures. The overall more bulky setup is prone to multiple scattering effects and can cause artefacts on the detector that are not sample related. This also requires more pronounced masking of the raw scattering data and leads to a decrease in counting statistics. The counting statistic is even more reduced due to the setup, as the capillary cannot be spun during the measurements. Furthermore, the setup does not allow to move both the shielding lead tube of the incoming beam as well as the beam stop as close to the sample as possible for the ex situ measurements, which leads to a lower reduction of air scattering. As a gas flow through the sample capillary has to be ensured, it was necessary to press the powder into small pellets (150–250 μm). Therefore, an optimized dense filling and material compaction as it was obtained for the *ex situ* samples could not be maintained. This also increases the risk of different material packing and can cause density differences and related effects. The presence of the gas atmosphere itself (Ar or H_2 and ethylene in Ar) will also cause

additional scattering effects further diluting the scattering signal of the immobilized metal species. As the temperature is increased, thermal motion has to be considered another influencing factor.

It is demonstrated in Fig. S19 how the above mentioned factors influence the data quality of a RT measurement obtained from the *in situ* setup with an Ar flow in comparison with an *ex situ* measurement of pure ECN support material. The F(Q) of the *in situ* data clearly contains more noise starting from lower Q-values (~12 $Å^{-1}$). In order to avoid data with high levels of noise in the further data reduction procedure, the total scattering data of the *in situ* measurements were truncated at a Q_{max} of 13 $Å^{-1}$ and a $Q_{maxinst}$ of 17 $Å^{-1}$. This however comes at the cost of real space resolution and has to be carefully considered during data evaluation.

8. Conclusion

In order to be able to assign catalytic activity and selectivity to a certain metal species and its chemical and geometrical surrounding, it is inevitable to discover different tools for their detailed characterization and the determination of atomic dispersion especially under reaction conditions. Generally, high-energy synchrotron X-ray total scattering (TS) and atomic (difference) pair distribution function (PDF) analysis allows the extraction of structural information on different length scales and with respect to multiple elements at the same time. This can be particularly important as not only the metal species but also the structure of the carbonaceous support materials, which act as macroligands are known to influence catalytic activity.

In this study, we demonstrate the applicability of high-energy synchrotron TS and atomic (difference) pair distribution function analysis (dPDF) for the local structure determination of low-loading single-atom catalysts based on carbonaceous polymeric support materials. Information on the first coordination shell of the immobilized metal species can be obtained via this analysis method, as well as further coordination shells when the complex with the support material is sufficiently well defined. The presence, absence or shifts of certain atom pair correlation peaks have the potential to contribute to the understanding of the catalyst's local bonding environment. Like XAS, X-ray TS is a bulk average characterization method. However, it is not element specific, so the dominating contribution from the support material must either be modeled or removed to improve sensitivity to the complex structure contribution of the catalyst. This can be reasonably achieved by difference PDF analysis. However, as the target signals are generally a very small at operationally relevant loading, appropriate sample preparation, data acquisition and processing procedure are decisive. The resulting high quality data need to have a high signal-to-noise ratio and very good counting statistics in order to enable an accurate background subtraction and reveal the desired structural information. Synchrotron radiation while substantially better than laboratory anodes, still does not automatically guarantee high-quality data. Nevertheless, it was shown that high-energy synchrotron radiation is needed for the analysis of these systems and that data obtained with laboratory instruments did not lead to reliable dPDFs even with optimized capillary preparation.

The absence of metal-metal pair correlations in the dPDFs of the single-atom catalyst samples indicated a successful dispersion of isolated metal sites. This is in accordance with XPS analysis where no contribution of metallic Pd could be detected. A change in the coordination environment of the metal species depending on the precursor used could be identified by the presence of characteristic pair correlations at only 0.5 wt% metal loading. Pair correlations based on highly scattering atom pairs (metal-metal) will provide increased scattering contribution relative to the pair correlations based on metal-X or from within the support, meaning that there should be enhanced sensitivity to agglomerated particles. Furthermore, depending on the difference between scattering intensities of the ligand-atoms and the atoms in the support material it is challenging to distinguish their contributions in the dPDFs. The comparison with DFT-optimized model structures and the PDF measurements of reference materials representing different potential coordination scenarios is of great value for the dPDF peak assignment.

This work is a demonstration of the importance of following the structural evolution under reaction conditions in order to correctly identify catalytically active sites. Especially, in consideration of potential sample contamination and air exposure to cover and alter the sensitive local and electronic structure information of very dilute samples. Quasi *in situ* XPS measurements revealed the formation of an additional electron-rich Pd species (matching Pd^0) after a treatment at 100 °C in a reductive atmosphere, coinciding with the emergence of catalytic activity as reported by Vennewald et al. [14]. With continuing course of reaction the formed species grows and dominates the spectrum after an exposure to 350 °C. The *in situ* dPDF analysis confirms the Pd nanoparticle formation via distinct Pd–Pd pair correlations that are visible at 350 °C. The consistent dPDF trends observed with temperature and time are in line with findings of the XPS analysis.

This work aims at promoting the application of X-ray total scattering and PDF analysis as a complementary method to an already well-established portfolio for the characterization of heterogeneous catalysts such as X-ray absorption spectroscopy or electron microscopy. The studies demonstrate the enormous potentials of the method but also its limitations, especially under the consideration of dPDF analysis. Results from systematic studies of how sample preparation and measuring strategies affect results are important for weak scattering polymeric catalysts but also in general. We would like to support future potential users of this method by providing measurement guidelines, so that they can make full use of this method and contribute to the unravelling of local structure information in high performance materials at ambient, but more importantly, at working conditions.

CRediT authorship contribution statement

Isabella Kappel: Writing – original draft, Validation, Project administration, Methodology, Investigation, Formal analysis. **Maxwell W. Terban:** Writing – review & editing, Validation, Software. **Maurice Vennewald:** Resources, Conceptualization. **Nina M. Sackers:** Methodology. **Andree Iemhoff:** Resources, Conceptualization. **Janine C. Baums:** Resources. **Sebastian Leiting:** Investigation. **Martin Etter:** Resources, Investigation. **Peter J.C. Hausoul:** Writing – review & editing, Supervision. **Regina Palkovits:** Writing – review & editing, Supervision, Funding acquisition, Conceptualization. **Claudia Weidenthaler:** Writing – review & editing, Supervision, Resources, Methodology, Conceptualization.

Associated content

Additional experimental details, materials, and methods, including photographs of experimental setup (DOC). This material is available free of charge via the Internet at http://pubs.acs.org."

Funding sources

Any funds used to support the research of the manuscript should be placed here (per journal style).NotesAny additional relevant notes should be placed here.

Declaration of competing interest

The authors declare the following financial interests/personal relationships which may be considered as potential competing interests: Regina Palkovits reports financial support was provided by Deutsche Forschungsgemeinschaft (DFG, German Research Foundation). If there are other authors, they declare that they have no known competing financial interests or personal relationships that could have appeared to influence the work reported in this paper.

Acknowledgment

This study was supported by the Deutsche Forschungsgemeinschaft (DFG, German Research Foundation) under Germany's Excellence Strategy within the Exzellenzcluster 2186 "The Fuel Science Center" ID:390919832. IK would like to thank Simon Billinge for valuable discussions and technical suggestions. We acknowledge DESY (Hamburg, Germany), a member of the Helmholtz Association HGF, for the provision of experimental facilities. Parts of this research were carried out at PETRA III beamline P02.1. Thanks also to Dr. Alba San Jose Mendez for her support at beamline P02.1, PETRA III, DESY, Hamburg.

Appendix A. Supplementary data

Supplementary data to this article can be found online at https://doi.org/10.1016/j.mtchem.2025.102776.

Data availability

Data will be made available on request.

References

[1] J. Artz, Covalent triazine-based frameworks—tailor-made catalysts and catalyst supports for molecular and nanoparticulate species, ChemCatChem 10 (8) (2018) 1753–1771, https://doi.org/10.1002/cctc.201701820.
[2] X.-F. Yang, A. Wang, B. Qiao, J. Li, J. Liu, T. Zhang, Single-atom catalysts: a new frontier in heterogeneous catalysis 46 (8) (2013) 1740–1748.
[3] X. Li, X. Yang, J. Zhang, Y. Huang, B. Liu, In situ/operando techniques for characterization of single-atom catalysts, ACS Catal. 9 (3) (2019) 2521–2531, https://doi.org/10.1021/acscatal.8b04937.
[4] M. Kottwitz, Y.Y. Li, H.D. Wang, A.I. Frenkel, R.G. Nuzzo, Single atom catalysts: a review of characterization methods, Chem. Methods 1 (6) (2021) 278–294, https://doi.org/10.1002/cmtd.202100020.
[5] P. Qi, J. Wang, X. Djitcheu, D. He, H. Liu, Q. Zhang, Techniques for the characterization of single atom catalysts, RSC Adv. 12 (2) (2022) 1216–1227, https://doi.org/10.1039/D1RA07799F.
[6] G.F.R. Rocha, M.A. da Silva, A. Rogolino, G.A. Diab, L.F. Noleto, M. Antonietti, I. F. Teixeira, Carbon nitride based materials: more than just a support for single-atom catalysis, Chem. Soc. Rev. (2023), https://doi.org/10.1039/D2CS00806H.
[7] S.K. Kaiser, Z. Chen, D. Faust Akl, S. Mitchell, J. Perez-Ramirez, Single-atom catalysts across the periodic table, Chem. Rev. 120 (21) (2020) 11703–11809, https://doi.org/10.1021/acs.chemrev.0c00576.
[8] J. Li, Q. Guan, H. Wu, W. Liu, Y. Lin, Z. Sun, X. Ye, X. Zheng, H. Pan, J. Zhu, S. Chen, W. Zhang, S. Wei, J. Lu, Highly active and stable metal single-atom catalysts achieved by strong electronic metal-support interactions, J. Am. Chem. Soc. 141 (37) (2019) 14515–14519, https://doi.org/10.1021/jacs.9b06482.
[9] A. Uzun, V. Ortalan, N.D. Browning, B.C. Gates, Site-isolated iridium complexes on MgO powder: individual Ir atoms imaged by scanning transmission electron microscopy, Chem. Commun. (31) (2009) 4657–4659, https://doi.org/10.1039/b823171k.
[10] A. Uzun, V. Ortalan, N.D. Browning, B.C. Gates, A site-isolated mononuclear iridium complex catalyst supported on MgO: characterization by spectroscopy and aberration-corrected scanning transmission electron microscopy, J. Catal. 269 (2) (2010) 318–328, https://doi.org/10.1016/j.jcat.2009.11.017.
[11] B. Qiao, A. Wang, X. Yang, L.F. Allard, Z. Jiang, Y. Cui, J. Liu, J. Li, T. Zhang, Single-atom catalysis of CO oxidation using Pt1/FeOx, Nat. Chem. 3 (8) (2011) 634–641, https://doi.org/10.1038/nchem.1095.
[12] A.V. Crewe, J. Wall, J. Langmore, Visibility of single atoms, Sci. Technol. Humanit. 168 (3937) (1970) 1338–1340, https://doi.org/10.1126/science.168.3937.1338.
[13] N. Dellby, O.L. Krivanek, P.D. Nellist, P.E. Batson, A.R. Lupini, Progress in aberration-corrected scanning transmission electron microscopy, J. Electron. Microsc. 50 (3) (2001) 177–185, https://doi.org/10.1093/jmicro/50.3.177.
[14] M. Vennewald, N.M. Sackers, A. Iemhoff, I. Kappel, C. Weidenthaler, A. Meise, M. Heggen, R.E. Dunin-Borkowski, L. Keenan, R. Palkovits, Dynamics of palladium single-atoms on graphitic carbon nitride during ethylene hydrogenation, J. Catal. 421 (2023) 134–144, https://doi.org/10.1016/j.jcat.2023.03.011.
[15] S.K. Kaiser, I. Surin, A. Amoros-Perez, S. Buchele, F. Krumeich, A.H. Clark, M. C. Roman-Martinez, M.A. Lillo-Rodenas, J. Perez-Ramirez, Design of carbon supports for metal-catalyzed acetylene hydrochlorination, Nat. Commun. 12 (1) (2021) 4016, https://doi.org/10.1038/s41467-021-24330-2.
[16] S. Buchele, A. Yakimov, S.M. Collins, A. Ruiz-Ferrando, Z. Chen, E. Willinger, D. M. Kepaptsoglou, Q.M. Ramasse, C.R. Muller, O.V. Safonova, N. Lopez, C. Coperet, J. Perez-Ramirez, S. Mitchell, Elucidation of metal local environments in single-atom catalysts based on carbon nitrides, Small (Weinh.) 18 (33) (2022) e2202080, https://doi.org/10.1002/smll.202202080.
[17] M. Kottwitz, Y. Li, H. Wang, A.I. Frenkel, R.G.J.C.M. Nuzzo, Single atom catalysts: a review of characterization methods 1 (6) (2021) 278–294.
[18] G. Malta, S.A. Kondrat, S.J. Freakley, C.J. Davies, L. Lu, S. Dawson, A. Thetford, E. K. Gibson, D.J. Morgan, W. Jones, P.P. Wells, P. Johnston, C.R. Catlow, C.J. Kiely, G.J. Hutchings, Identification of single-site gold catalysis in acetylene hydrochlorination, Sci. Technol. Humanit. 355 (6332) (2017) 1399–1403, https://doi.org/10.1126/science.aal3439.
[19] L. Liu, D.M. Meira, R. Arenal, P. Concepcion, A.V. Puga, A. Corma, Determination of the evolution of heterogeneous single metal atoms and nanoclusters under reaction conditions: which are the working catalytic sites? ACS Catal. 9 (12) (2019) 10626–10639, https://doi.org/10.1021/acscatal.9b04214.
[20] E. Vorobyeva, E. Fako, Z. Chen, S.M. Collins, D. Johnstone, P.A. Midgley, R. Hauert, O.V. Safonova, G. Vile, N. Lopez, S. Mitchell, J. Perez-Ramirez, Atom-by-Atom resolution of structure-function relations over low-nuclearity metal catalysts, Angew Chem. Int. Ed. Engl. 58 (26) (2019) 8724–8729, https://doi.org/10.1002/anie.201902136.
[21] Z.P. Chen, S. Mitchell, E. Vorobyeva, R.K. Leary, R. Hauert, T. Furnival, Q. M. Ramasse, J.M. Thomas, P.A. Midgley, D. Dontsova, M. Antonietti, S. Pogodin, N. López, J. Pérez-Ramírez, Stabilization of single metal atoms on graphitic carbon nitride, Adv. Funct. Mater. 27 (8) (2017) 1605785, https://doi.org/10.1002/adfm.201605785.
[22] A. Iemhoff, J. Deischter, S. Jung, G. Tuci, G. Giambastiani, R. Palkovits, Polymer-inspired covalent triazine frameworks from the carbonaceous side - influence of unexpected surface functionalisation on liquid-phase adsorption processes, J. Mater. Chem. A 9 (9) (2021) 5390–5403, https://doi.org/10.1039/d0ta10195h.
[23] X. Hai, S.B. Xi, S. Mitchell, K. Harrath, H.M. Xu, D.F. Akl, D.B. Kong, J. Li, Z.J. Li, T. Sun, H.M. Yang, Y.G. Cui, C.L. Su, X.X. Zhao, J. Li, J. Pérez-Ramírez, J. Lu, Scalable two-step annealing method for preparing ultra-high-density single-atom catalyst libraries, Nat. Nanotechnol. 17 (2022) 174, https://doi.org/10.1038/s41565-021-01022-y, 17(3) (2022) 331-331.
[24] N.M. Sackers, A. Iemhoff, P. Sautet, R.J.C.S. Palkovits, Technology, Understanding the Structure of Isolated Iridium Sites Anchored on a Covalent Triazine Framework, 2023.
[25] S.J. Billinge, I. Levin, The problem with determining atomic structure at the nanoscale, Sci. Technol. Humanit. 316 (5824) (2007) 561–565, https://doi.org/10.1126/science.1135080.
[26] T.L. Christiansen, S.R. Cooper, K.M.J.N.A. Jensen, There's no place like real-space: elucidating size-dependent atomic structure of nanomaterials using pair distribution function analysis, Nanoscale Adv. 2 (6) (2020) 2234–2254, https://doi.org/10.1039/D0NA00120A.
[27] I. Romero-Muñiz, A. Mavrandonakis, P. Albacete, A. Vega, V. Briois, F. Zamora, A. E. Platero-Prats, Unveiling the local structure of palladium loaded into imine-linked layered covalent organic frameworks for cross, Coupling Catalysis 59 (31) (2020) 13013–13020.
[28] M.W. Terban, S.J.L. Billinge, Structural analysis of molecular materials using the pair distribution function, Chem. Rev. 122 (1) (2022) 1208–1272, https://doi.org/10.1021/acs.chemrev.1c00237.
[29] M.W. Terban, M. Johnson, M. Di Michiel, S.J.J.N. Billinge, Detection and characterization of nanoparticles in suspension at low concentrations using the X-ray total scattering pair distribution function technique, Nanoscale 7 (12) (2015) 5480–5487, https://doi.org/10.1039/C4NR06486K.
[30] K.W. Chapman, P.J. Chupas, C.J. Kepert, Selective recovery of dynamic guest structure in a nanoporous prussian blue through in situ X-ray diffraction: a differential pair distribution function analysis, J. Am. Chem. Soc. 127 (32) (2005) 11232–11233, https://doi.org/10.1021/ja053266k.
[31] K.W. Chapman, P.J. Chupas, E.R. Maxey, J.W. Richardson, Direct observation of adsorbed H 2-framework interactions in the Prussian Blue analogue Mn II 3 [Co III (CN) 6] 2: The relative importance of accessible coordination sites and van der Waals interactions, Chem. Commun. (38) (2006) 4013–4015, https://doi.org/10.1039/B607250J.
[32] C. Castillo-Blas, J.M. Moreno, I. Romero-Muñiz, A.E.J.N. Platero-Prats, Applications of pair distribution function analyses to the emerging field of non-ideal metal–organic framework materials, Nanoscale 12 (29) (2020) 15577–15587, https://doi.org/10.1039/D0NR01673J.
[33] M.W. Terban, S.K. Ghose, A.M. Plonka, D. Troya, P. Juhás, R.E. Dinnebier, J. J. Mahle, W.O. Gordon, A.I. Frenkel, Atomic resolution tracking of nerve-agent simulant decomposition and host metal–organic framework response in real space, Commun. Chem. 4 (1) (2021) 2, https://doi.org/10.1038/s42004-020-00439-1.
[34] M.W. Terban, C. Shi, R. Silbernagel, A. Clearfield, S.J.J.I.C. Billinge, Local environment of terbium (III) ions in layered nanocrystalline zirconium (IV) phosphonate–phosphate ion exchange materials 56 (15) (2017) 8837–8846.
[35] L. Liu, A. Corma, Bimetallic sites for catalysis: from binuclear metal sites to bimetallic nanoclusters and nanoparticles, Chem. Rev. 123 (8) (2023) 4855–4933, https://doi.org/10.1021/acs.chemrev.2c00733.
[36] J.E. Mondloch, E. Bayram, R.G. Finke, A review of the kinetics and mechanisms of formation of supported-nanoparticle heterogeneous catalysts, J. Mol. Catal. Chem. 355 (2012) 1–38, https://doi.org/10.1016/j.molcata.2011.11.011.
[37] K.O. Sulaiman, M. Zubair, G. King, N.M. Bedford, R.W. Scott, Taking a different road: following Ag 25 and Au 25 cluster activation via in situ differential pair distribution function analysis, Phys. Chem. Chem. Phys. 24 (40) (2022) 24834–24844, https://doi.org/10.1039/D2CP02682A.
[38] P.J. Chupas, K.W. Chapman, G. Jennings, P.L. Lee, C.P. Grey, Watching nanoparticles grow: the mechanism and kinetics for the formation of TiO2-supported platinum nanoparticles, J. Am. Chem. Soc. 129 (45) (2007) 13822–13824, https://doi.org/10.1021/ja076437p.
[39] P.J. Chupas, K.W. Chapman, H. Chen, C.P. Grey, Application of high-energy X-rays and Pair-Distribution-Function analysis to nano-scale structural studies in catalysis,

Catal. Today 145 (3–4) (2009) 213–219, https://doi.org/10.1016/j.cattod.2009.03.026.
[40] M.A. Newton, K.W. Chapman, D. Thompsett, P.J. Chupas, Chasing changing nanoparticles with time-resolved pair distribution function methods, J. Am. Chem. Soc. 134 (11) (2012) 5036–5039, https://doi.org/10.1021/ja2114163.
[41] I. Romero-Muniz, A. Mavrandonakis, P. Albacete, A. Vega, V. Briois, F. Zamora, A. E. Platero-Prats, Unveiling the local structure of palladium loaded into imine-linked layered covalent organic frameworks for cross-coupling catalysis, Angew Chem. Int. Ed. Engl. 59 (31) (2020) 13013–13020, https://doi.org/10.1002/anie.202004197.
[42] Z. Chen, S.M. Gulam Rabbani, Q. Liu, W. Bi, J. Duan, Z. Lu, N.M. Schweitzer, R. B. Getman, J.T. Hupp, K.W. Chapman, Atomically precise single-site catalysts via exsolution in a polyoxometalate–metal–organic-framework architecture, J. Am. Chem. Soc. 146 (12) (2024) 7950–7955, https://doi.org/10.1021/jacs.4c00523.
[43] T. Qin, L. Li, X. Mu, X. Liu, L. Chen, Structural evolution of supported Pt atoms during calcination using electron atomic pair distribution function: implications for catalysis, ACS Appl. Nano Mater. 7 (17) (2024) 20474–20483, https://doi.org/10.1021/acsanm.4c03294.
[44] A. Iemhoff, M. Vennewald, J. Artz, C. Mebrahtu, A. Meledin, T.E. Weirich, H. Hartmann, A. Besmehn, M. Aramini, F.J.C. Venturini, On the stability of isolated iridium sites in N-rich frameworks against agglomeration under reducing conditions, ChemCatChem 14 (9) (2022) e202200179, https://doi.org/10.1002/cctc.202200179.
[45] R. Sun, A. Kann, H. Hartmann, A. Besmehn, P.J. Hausoul, R. Palkovits, Direct synthesis of methyl formate from CO2 with phosphine-based polymer-bound Ru catalysts, ChemSusChem 12 (14) (2019) 3278–3285, https://doi.org/10.1002/cssc.201900808.
[46] A. Kann, H. Hartmann, A. Besmehn, P.J. Hausoul, R. Palkovits, Hydrogenation of CO2 to formate over ruthenium immobilized on solid molecular phosphines, ChemSusChem 11 (11) (2018) 1857–1865, https://doi.org/10.1002/cssc.201800413.
[47] P.J. Hausoul, C. Broicher, R. Vegliante, C. Goeb, R. Palkovits, Solid molecular phosphine catalysts for formic acid decomposition in the biorefinery, Angew. Chem. Int. Ed. 55 (18) (2016) 5597–5601, https://doi.org/10.1002/anie.201510681.
[48] J.C. Baums, I. Kappel, A. Meise, M. Heggen, C. Weidenthaler, P.J. Hausoul, R. Palkovits, Additive-free, aqueous CO2 hydrogenation with Ru/Polyphosphine-Based solid molecular catalysts, ChemCatChem (2025) e202402048, https://doi.org/10.1002/cctc.202402048.
[49] A. Iemhoff, M. Vennewald, R. Palkovits, Single-atom catalysts on covalent triazine frameworks: at the crossroad between homogeneous and heterogeneous catalysis, Angew. Chem. Int. Ed. 62 (7) (2023) e202212015, https://doi.org/10.1002/anie.202212015.
[50] P. Kuhn, M. Antonietti, A. Thomas, Porous, covalent triazine-based frameworks prepared by ionothermal synthesis, Angew. Chem. Int. Ed. 47 (18) (2008) 3450–3453, https://doi.org/10.1002/anie.200705710.
[51] P. Kuhn, A. Thomas, M. Antonietti, Toward tailorable porous organic polymer networks: a high-temperature dynamic polymerization scheme based on aromatic nitriles, Macromolecules 42 (1) (2009) 319–326, https://doi.org/10.1021/ma802322j.
[52] M. Vennewald, Untersuchung der Dynamiken von Palladium-Einzelatomen auf graphitischem Kohlenstoffnitrid in Hydrierungsreaktionen, RWTH Aachen University, Dissertation, 2023.
[53] S.L. Thomae, N. Prinz, T. Hartmann, M. Teck, S. Correll, M. Zobel, Pushing data quality for laboratory pair distribution function experiments, Rev. Sci. Instrum. 90 (4) (2019) 043905, https://doi.org/10.1063/1.5093714.
[54] P.J. Chupas, X. Qiu, J.C. Hanson, P.L. Lee, C.P. Grey, S.J. Billinge, Rapid-acquisition pair distribution function (RA-PDF) analysis, J. Appl. Crystallogr. 36 (6) (2003) 1342–1347.
[55] H. King, F. Manchester, A low-temperature X-ray diffraction study of Pd and some Pd-H alloys, J. Phys. F Met. Phys. 8 (1) (1978) 15, https://doi.org/10.1088/0305-4608/8/1/007.
[56] T. Egami, S.J. Billinge, Underneath the Bragg Peaks: Structural Analysis of Complex Materials, Elsevier, 2003.
[57] T. Proffen, S. Billinge, T. Egami, D. Louca, Structural analysis of complex materials using the atomic pair distribution function—a practical guide, Z. Kristallogr. Cryst. Mater. 218 (2) (2003) 132–143, https://doi.org/10.1524/zkri.218.2.132.20664.
[58] B. Toby, T. Egami, Accuracy of pair distribution function analysis applied to crystalline and non-crystalline materials, Acta Crystallogr., Sect. A: Found. Crystallogr. 48 (3) (1992) 336–346.
[59] P. Juhás, T. Davis, C.L. Farrow, S.J. Billinge, PDFgetX3: a rapid and highly automatable program for processing powder diffraction data into total scattering pair distribution functions, J. Appl. Crystallogr. 46 (2) (2013) 560–566, https://doi.org/10.1107/S0021889813005190.
[60] S.J. Billinge, C.L. Farrow, Towards a robust ad hoc data correction approach that yields reliable atomic pair distribution functions from powder diffraction data, J. Phys. Condens. Matter 25 (45) (2013) 454202, https://doi.org/10.1088/0953-8984/25/45/454202.
[61] F. Fina, S.K. Callear, G.M. Carins, J.T.S. Irvine, Structural investigation of graphitic carbon nitride via XRD and neutron diffraction, Chem. Mater. 27 (7) (2015) 2612–2618, https://doi.org/10.1021/acs.chemmater.5b00411.
[62] H. Schlomberg, J. Kröger, G. Savasci, M.W. Terban, S. Bette, I. Moudrakovski, V. Duppel, F. Podjaski, R. Siegel, J. Senker, R.E. Dinnebier, C. Ochsenfeld, B. V. Lotsch, Structural insights into poly(Heptazine Imides): a light-storing carbon nitride material for dark photocatalysis, Chem. Mater. 31 (18) (2019) 7478–7486, https://doi.org/10.1021/acs.chemmater.9b02199.
[63] J. Kröger, F. Podjaski, G. Savasci, I. Moudrakovski, A. Jiménez-Solano, M. W. Terban, S. Bette, V. Duppel, M. Joos, A. Senocrate, Conductivity mechanism in ionic 2D carbon nitrides: from hydrated ion motion to enhanced photocatalysis, Adv. Mater. 34 (7) (2022) 2107061, https://doi.org/10.1002/adma.202107061.
[64] P. Coppens, Comparative X-ray and neutron diffraction study of bonding effects in s-triazine, Sci. Technol. Humanit. 158 (3808) (1967) 1577–1579, https://doi.org/10.1126/science.158.3808.1577.
[65] M.W. Terban, K. Seidel, E. Pöselt, M. Malfois, R.-P. Baumann, R. Sander, D. Paulus, B. Hinrichsen, R.E. Dinnebier, Cross-examining polyurethane nanodomain formation and internal structure, Macromolecules 53 (20) (2020) 9065–9073, https://doi.org/10.1021/acs.macromol.0c01557.
[66] M.W. Terban, A.M. Pütz, G. Savasci, U. Heinemeyer, B. Hinrichsen, P. Desbois, R. E. Dinnebier, Improving the picture of atomic structure in nonoriented polymer domains using the pair distribution function: a study of polyamide 6, J. Polym. Sci. 58 (13) (2020) 1843–1866, https://doi.org/10.1002/pol.20190272.
[67] A.M. Pütz, M.W. Terban, S. Bette, F. Haase, R.E. Dinnebier, B.V. Lotsch, Total scattering reveals the hidden stacking disorder in a 2D covalent organic framework, Chem. Sci. 11 (47) (2020) 12647–12654, https://doi.org/10.1039/D0SC03048A.
[68] L. Gamez-Mendoza, M.W. Terban, S.J. Billinge, M. Martinez-Inesta, Modelling and validation of particle size distributions of supported nanoparticles using the pair distribution function technique, J. Appl. Crystallogr. 50 (3) (2017) 741–748, https://doi.org/10.1107/S1600576717003715.
[69] P. Juhas, C.L. Farrow, X. Yang, K.R. Knox, S.J. Billinge, Complex modeling: a strategy and software program for combining multiple information sources to solve ill posed structure and nanostructure inverse problems, Acta Crystallogr. A Found. Adv. 71 (Pt 6) (2015) 562–568, https://doi.org/10.1107/S2053273315014473.
[70] D. Zagorac, H. Müller, S. Ruehl, J. Zagorac, S. Rehme, Recent developments in the Inorganic Crystal Structure Database: theoretical crystal structure data and related features, J. Appl. Crystallogr. 52 (5) (2019) 918–925, https://doi.org/10.1107/S160057671900997X.
[71] W. Theilacker, Die Anordnung der Valenzen im koordinativ 4-wertigen Palladium und Platin Anhang: Die Kristallstruktur des Kaliumpalladochlorids, Z. Anorg. Allg. Chem. 234 (2) (1937) 161–178, https://doi.org/10.1002/zaac.19372340208.
[72] J. Hester, E. Maslen, N. Spadaccini, N. Ishizawa, Y. Satow, Accurate synchrotron radiation [Delta][rho] maps for K [sub 2] SiF [sub 6] and K [sub 2] PdCl [sub 6], Acta Crystallogr. B, Structural Science;(Denmark) 49 (6) (1993), https://doi.org/10.1107/S0108768193005725.
[73] J. Waser, H.A. Levy, S. Peterson, The structure of PdO, Acta Crystallogr. 6 (7) (1953) 661–663, https://doi.org/10.1107/s0365110x53001800.
[74] B. Dickinson, The crystal structure of tetramminopalladous chloride Pd (NH3) 4Cl2· H2O, Z. Kristallogr. Cryst. Mater. 88 (1–6) (1934) 281–297, https://doi.org/10.1524/zkri.1934.88.1.281.
[75] K. Ha, Dichlorido (1, 10-phenanthroline-κ2N, N′) palladium (II), Acta Crystallogr. E: Structure Reports Online 66 (1) (2010), https://doi.org/10.1107/S1600536809052313 m38-m38.
[76] Y. Urashima, T. Wakabayashi, T. Masaki, Y. Terasaki, Ruthenium, a new mineral from Horokanai, Hokkaido, Japan, Mineral. J. 7 (5) (1974) 438–444, https://doi.org/10.2465/minerj1953.7.438.
[77] K.S. Kim, A. Gossmann, N. Winograd, X-ray photoelectron spectroscopic studies of palladium oxides and the palladium-oxygen electrode, Anal. Chem. 46 (2) (1974) 197–200.
[78] W.P. Zhou, A. Lewera, R. Larsen, R.I. Masel, P.S. Bagus, A. Wieckowski, Size effects in electronic and catalytic properties of unsupported palladium nanoparticles in electrooxidation of formic acid, J. Phys. Chem. B 110 (27) (2006) 13393–13398, https://doi.org/10.1021/jp061690h.
[79] S. Hofmann, in: Auger-and X-Ray Photoelectron Spectroscopy in Materials Science: a User-Oriented Guide, Springer Science & Business Media, 2012, https://doi.org/10.1007/978-3-642-27381-0.
[80] A. Iemhoff, M.S. Rose, R. Palkovits, Stabilisierte Einzelatome in der Katalyse: Einfluss stickstoffhaltiger Trägermaterialien am Beispiel kovalenter Triazin-basierter Netzwerke, Fachgruppe Chemie, 2022.
[81] L.B. Skinner, C.J. Benmore, J.B. Parise, Area detector corrections for high quality synchrotron X-ray structure factor measurements, Nucl. Instrum. Methods Phys. Res. 662 (1) (2012) 61–70, https://doi.org/10.1016/j.nima.2011.09.031.